

RICE UNIVERSITY

**Ultrafast and Magneto-optical Spectroscopy of  
Excitons and Phonons in Carbon Nanotubes**

by

**Layla Goli Booshehri**

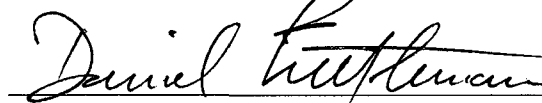
A THESIS SUBMITTED  
IN PARTIAL FULFILLMENT OF THE  
REQUIREMENTS FOR THE DEGREE

**Master of Science**

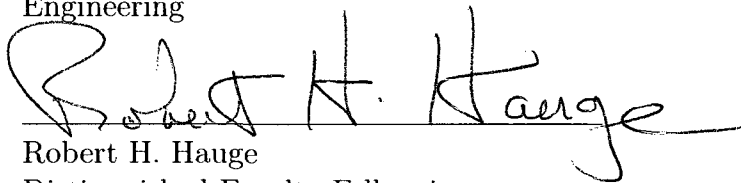
APPROVED, THESIS COMMITTEE:



Junichiro Kono, Chair  
Professor of Electrical & Computer  
Engineering and Physics & Astronomy



Daniel M. Mittleman  
Professor of Electrical & Computer  
Engineering



Robert H. Hauge  
Distinguished Faculty Fellow in  
Chemistry

Houston, Texas

June, 2010

UMI Number: 1486557

All rights reserved

**INFORMATION TO ALL USERS**

The quality of this reproduction is dependent upon the quality of the copy submitted.

In the unlikely event that the author did not send a complete manuscript and there are missing pages, these will be noted. Also, if material had to be removed, a note will indicate the deletion.



UMI 1486557

Copyright 2010 by ProQuest LLC.

All rights reserved. This edition of the work is protected against unauthorized copying under Title 17, United States Code.



ProQuest LLC  
789 East Eisenhower Parkway  
P.O. Box 1346  
Ann Arbor, MI 48106-1346

## ABSTRACT

### Ultrafast and Magneto-optical Spectroscopy of Excitons and Phonons in Carbon Nanotubes

by

Layla Goli Booshehri

Understanding how electrons and phonons relax in energy and momentum is one of the current goals in carbon nanotube spectroscopy as well as an important step toward developing novel electronic and optoelectronic devices based on carbon nanotubes. Here, we investigate the polarization anisotropy of coherent phonon (CP) dynamics of radial breathing mode (RBM) phonons in highly-aligned single-walled carbon nanotubes (SWNTs). Using CP spectroscopy, we measure RBM CPs as a function of angle for two different geometries and in both cases, we observe quenching of the RBM when polarization is perpendicular to the nanotubes. We also make progress in understanding the role of dark excitons in SWNTs at ultralow temperatures. Measuring the magnetic field dependence to 5 T, we obtained an unexpected zero-field photoluminescence (PL) and PL brightening at 50 mK. To explain this contradiction with current theory, we introduced a non-thermal distribution of excitons into current theory.

## Acknowledgments

I would like to begin by first thanking my advisor, Professor Junichiro Kono, for his never-ending support and encouragement throughout the course of this work. His advice and guidance have not only allowed for the completion of these experiments, but they have also provided the foundation for my academic pursuits. Secondly, I would like to thank my mother, father, and sister (sissy). They are my source of inspiration, my strength, and my heart. They make this journey forever worthwhile.

I would like to especially thank Dr. Chanjuan Sun for not only her mentorship and the many, many hours she dedicated to teach me both experimental and theoretical techniques, but also for her fellow “girl-power” solidarity. I would also like to thank Dr. Ajit Srivastava for being my unofficial mentor when I joined the Kono group and for his detective skills in the lab when the experiment refused to work. I would like to express my gratitude to Thomas Searles for his constant guidance on everything Japan, PL, and “tubes”, and to Erik Haroz for always sharing his nanotube expertise. To Cary Pint, thank you for the many samples you made for my experiments and for your friendship and awesome collaborator-ship.

I am also grateful to all of the Kono group members and my colleagues that have made my graduate experience memorable, and to my collaborators from Tohoku University, Konkuk University, and Chungnam National University for hosting me overseas and providing the many resources and guidance for my experiments. Finally, I would like to thank Dr. Daniel Mittleman and Dr. Robert Hauge for agreeing to be on my thesis committee.

# Contents

Abstract	ii
Acknowledgments	iii
List of Illustrations	vi
<b>1 Introduction</b>	<b>1</b>
<b>2 Excitons and Phonons in SWNTs</b>	<b>3</b>
2.1 SWNT band structure . . . . .	3
2.2 Excitons in SWNTs . . . . .	6
2.3 Radiative decay in SWNTs . . . . .	8
2.4 SWNT band structure in magnetic field . . . . .	11
2.5 Symmetry breaking effect on radiative decay . . . . .	11
2.6 Phonons in carbon nanotubes . . . . .	13
<b>3 Magnetic Brightening of Dark Excitons</b>	<b>16</b>
3.1 Previous magnetic brightening measurements . . . . .	17
3.2 Experimental methods . . . . .	20
3.2.1 Dilution refrigeration . . . . .	20
3.2.2 mKelvin photoluminescence spectroscopy . . . . .	23
3.3 Experimental Results . . . . .	27
3.4 Analysis and Discussion . . . . .	30

<b>4 Polarization Dependent Coherent Phonon Spectroscopy</b>	<b>34</b>
4.1 Coherent Phonons . . . . .	35
4.2 Previous CP spectroscopy measurements . . . . .	39
4.3 Experimental methods . . . . .	46
4.3.1 Sample fabrication: Highly-aligned SWNTs . . . . .	46
4.3.2 Coherent phonon spectroscopy . . . . .	48
4.3.3 Polarization dependence . . . . .	55
4.4 Experimental results . . . . .	55
4.5 Analysis and discussion . . . . .	58
<b>5 Conclusion</b>	<b>65</b>
<b>Bibliography</b>	<b>66</b>

# Illustrations

2.1	Unrolled honeycomb lattice of a nanotube [20]. . . . .	4
2.2	The energy dispersion relation for 2D graphene. Conduction and valence bands are touching at K points indicating that graphene is a zero-gap semiconductor [19]. . . . .	5
2.3	1D energy dispersion for (a) (5,5) armchair nanotube, (b) (9,0) zigzag nanotube, and (c) (10,0) zigzag nanotube [19, 21, 22]. . . . .	6
2.4	Coulomb interactions giving rise to 16 partially degenerate exciton states in SWNTs. . . . .	7
2.5	(a) Relative energy of SWNT excitonic levels for the (10,0) nanotube [28]. (b) Singlet states: only 1 state is optically active. . . . .	8
2.6	(Left) Schematic of thermal population of excitons in systems of different dimensionality. (Right) Exciton energy dispersion. [27]. . . . .	9
2.7	(a) Radiative decay rate for excitons in SWNTs within the bright band only. (b) Radiative decay rate for excitons in SWNTs within the the singlet manifold. (Adapted from [31]). . . . .	10
2.8	Magnetic brightening of the dark singlet state when a symmetry breaking magnetic field is applied. (Adapted from [35]). . . . .	12
2.9	The phonon dispersion relation for graphite plotted along the high-symmetry in-plane directions [37]. . . . .	14

2.10 (a) Calculated phonon dispersion for (10,10) armchair nanotube. (b) Low-energy phonon dispersion curves for the (10,10) armchair nanotube [20]. . . . .	15
2.11 (Left) Out-of-plane tangential acoustic mode in graphene becomes (Right) the radial breathing mode optical phonon for SWNTs [20]. . . . .	15
3.1 Near band-edge absorption in semiconducting SWNTs in high magnetic fields for (a) polarization parallel to B and (b) both parallel and perpendicular to B [35]. . . . .	18
3.2 Temperature dependence of magnetic brightening as a function of (a) temperature (b) magnetic field [36]. . . . .	19
3.3 Micro-magneto PL of a single nanotube when the magnetic field is (a) parallel (b) perpendicular to the nanotube axis [38]. . . . .	21
3.4 (a) Dilution refrigerator before refrigeration cycle. (b) Dilution refrigerator during refrigeration cycle [39]. . . . .	22
3.5 Oxford Kelvinox MX50 Dilution Refrigerator [40]. . . . .	24
3.6 Magnetic field dependent mK PL experimental configuration. LD: laser diode, M: mirror, BS: beamsplitter. . . . .	26
3.7 Diagram of cold finger with nanotube sample attached. OFHC: oxide-free, high conductivity copper wire. . . . .	27
3.8 Current Theory: Lowest lying bright and dark singlet states. At 50 mK, the thermal energy is much smaller than the dark-bright splitting. . . . .	28
3.9 Zero-field PL for (8,3) at 4.3 K and 50 mK. 50 mK PL is comparable to 4.3 K, unexpected with current theory. . . . .	29



3.10 (Left) Magnetic brightening of the PL spectrum for the (8,3) nanotube at 50 mK. (Right) Magnetic brightening for 50 mK compared with 4.3 K. . . . .	29
3.11 Fitting of current theory with various amounts of disorder to 50 mK magnetic brightening. . . . .	31
3.12 (a) Fitting of Equation 3.4 to the 50 mK magnetic brightening. (b) Fit results produce a value of 0.45 for R, indicating that 45% of the entire exciton population is still in the bright state at 50 mK. . . . .	33
4.1 (a), (c), (e) ISRS generation mechanism. (b), (d), (f) DECP generation mechanism [50]. . . . .	36
4.2 Transient reflectivity measurements and corresponding FT spectrum for (a) bismuth and (b) antimony [50, 54, 55]. . . . .	38
4.3 Oscillatory part of the reflectivity in Bi at 8 K and fit to double damped harmonic function [50, 54, 55]. . . . .	38
4.4 Transient reflectivity change and FT spectrum for (001) surface of single crystal type IIa diamond [50, 56]. . . . .	39
4.5 (a) Pump-probe time-domain data taken with 800 nm center wavelength. Inset displays coherent phonon oscillations in the time-domain. (b) CP phonon oscillations measured at five different photon energies. Traces offset for clarity [44]. . . . .	40
4.6 (Left) 3D plots of FFT of CP oscillations and RRS over an excitation range of 710-850nm. (Right) 2D spectra comparing CP to RRS for three different photon energies [44]. . . . .	41

4.7	(a) Differential transmission dynamics of SWNTs. Top panel, visible excitation energy (1.2-2.4eV), probe energy is 2.1eV. Both are sub-10-fs pulses. Bottom panel, 30-fs excitation pulse at 0.92eV and a sub-10-fs probe pulse with 2.0eV energy. (b) Vibrational spectra of SWNTs. Top panel is FFT of CP spectra from (a) and bottom panel is CW Raman spectrum for comparison [45]. . . . .	42
4.8	(a) (Left) Differential transmission of ensemble solution sample without pulse-shaping. (Right) FFT of time-domain oscillations with peak assignment. (b)-(f) (Left) Differential transmission of ensemble solution with pulse-shaping. (Right) FFT of selectively excited nanotubes [49]. . . . .	43
4.9	(Top) CP oscillations for various pump polarizations. (Bottom) Amplitude of CP oscillations for the (9,4) and (11,3) nanotubes as a function of pump polarization angle [46]. . . . .	45
4.10	(a) Transfer process scheme of aligned SWNT films (b) SEM image carpet arrays separated by 50 $\mu\text{m}$ prior to transfer process (c) complete transfer to diamond window[58]. . . . .	47
4.11	SWNT film diameter distribution[58]. . . . .	48
4.12	Schematic of coherent phonon spectroscopy system. . . . .	49
4.13	Schematic of A/D converter connections and fast scan detection. . . . .	51
4.14	Differential transmission of the time-domain pump-probe signal. Inset includes CP oscillations in the time-domain. . . . .	52
4.15	Oscillation of nanotube diameter and nanotube band gap. (a) As the nanotube diameter expands, the band gap shrinks. (b) As the nanotube diameter shrinks, the band gap expands. . . . .	53

4.16 (a) Time-domain signal of extracted CP oscillations. (b) FFT of time-domain of CP oscillations. . . . .	54
4.17 (a) UV-VIS Absorption spectrum of CVD grown aligned SWNTs at 0° and 90° to light polarization. (b) THz absorbance spectrum for the aligned SWNT film at 0° and 90° to THz polarization. . . . .	56
4.18 SEM image of aligned SWNTs and experimental configurations are shown. (a) For Type I, pump and probe polarizations are fixed and sample orientation is rotated. (b) For Type II, probe and sample orientations are fixed and pump polarization is rotated. . . . .	57
4.19 Polarization dependence of pump-probe signal in Type I orientation. .	58
4.20 Polarization dependence of CP signal in Type I orientation. . . . .	59
4.21 Polarization dependence of CP signal in Type II orientation. . . . .	60
4.22 Polarized CP spectrum for Type II. The traces are offset for clarity. .	61
4.23 Integrated CP intensity as a function of angle for Type I and Type II. The solid lines are fits to $\cos^4\theta$ , expected when nanotubes are perfectly aligned. . . . .	62
4.24 Misalignment effects on the integrated CP power [60]. . . . .	63
4.25 Experimental results fit to $A \cos^p(\theta + \Delta\theta) + B$ for Type I and $A \cos^p(\phi + \Delta\phi) + B$ for Type II [60]. . . . .	64

# Chapter 1

## Introduction

Since their discovery, much attention has been given to carbon nanotubes for their unique structure and promising nanotechnology applications. In particular, single-walled carbon nanotubes (SWNT) possess highly unusual electronic and optical properties, making them objects of great interest for basic scientific studies as well as potential applications [1]. Because of their direct band gaps, SWNTs are a leading candidate to unify electronic and optical functionality in the same nanoscale circuitry. The past several years have witnessed remarkable progress in our understanding of light emission and absorption processes in SWNTs, revealing the unusual properties of one-dimensional excitons and opening up possibilities for making SWNT-based optoelectronic devices including lasers.

More specifically, the one-dimensionality of single-walled carbon nanotubes is attractive from both fundamental and applied points of view, where the 1D confinement of electrons and phonons results in unique anisotropic electric, magnetic, mechanical, and optical properties. Individualized SWNTs, both single-tube and in ensemble samples, have shown anisotropy with polarized Raman and absorption measurements where maximum signals result when the nanotube axis is aligned parallel to the polarization of incident light [2, 3, 4, 5, 6, 7]. Additionally, due to strong anisotropic magnetic susceptibilities, both semiconducting and metallic SWNTs align well within an external magnetic field, and with the added properties of the Aharonov-Bohm effect, the electronic band structure of SWNTs respond anisotropically with the strength of

a tube-threading magnetic flux [8, 9, 10, 11, 12, 13, 14, 15]. Such optical and magnetic anisotropy is also expected with bulk samples, but detailed measurements showing extreme anisotropy have been lacking [16].

Here we present results on both mK magneto-photoluminescence (PL) and coherent phonon (CP) spectroscopy of SWNT thin films. We begin by providing a background on both excitons and phonons in Chapter 2, explaining the theory of radiative decay, magnetic brightening, and coherent phonons in SWNTs. In Chapter 3, we detail the experimental results and analysis of our mK magnetic brightening measurements, and extend current theory to include non-thermal distribution of excitons. Finally, in Chapter 4, we present our results on polarization dependent CP spectroscopy of highly-aligned SWNT thin films.

## Chapter 2

### Excitons and Phonons in SWNTs

#### 2.1 SWNT band structure

Single-walled carbon nanotubes (SWNTs) can be described as a single layer of graphite crystal (or graphene) that is rolled up into a seamless cylinder and has a very large aspect ratio, 1 nm vs. 100 nm [17]. Beginning with a 2D graphene sheet, shown in Figure 2.1, a nanotube can be specified by its chirality, how a nanotube is rolled, which is defined by the chiral vector

$$\vec{C}_h = n\vec{a}_1 + m\vec{a}_2 \equiv (n, m) \quad (2.1)$$

The chiral vector makes an angle  $\theta$  with the  $\vec{a}_1$  direction and connects sites  $O$  and  $A$ , where a carbon atom is located along the tube axis, lines  $OB$ ,  $AB'$  [18]. The unit vectors  $\vec{a}_1$  and  $\vec{a}_2$  define the unit cell of the honeycomb lattice and in real space are defined by

$$\vec{a}_1 = \left(\frac{\sqrt{3}}{2}a, \frac{a}{2}\right), \vec{a}_2 = \left(\frac{\sqrt{3}}{2}a, -\frac{a}{2}\right) \quad (2.2)$$

where  $a = |\vec{a}_1| = |\vec{a}_2| = 1.42 \times \sqrt{3} = 2.46 \text{ \AA}$  is the lattice constant of graphene [19]. The axis of the zigzag nanotube corresponds to  $\theta = 0^\circ$ , the armchair nanotube corresponds to  $\theta = 30^\circ$ , and the chiral nanotube corresponds to  $0^\circ < \theta < 30^\circ$ .

The 1D energy band structure for SWNTs is related to the 2D energy band structure calculated via the tight binding (TB) model for graphene. Using the TB approximation, wave functions in the honeycomb lattice can be represented by taking into

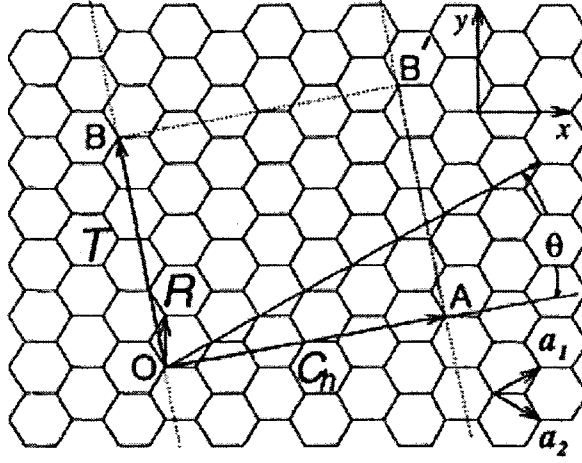


Figure 2.1 : Unrolled honeycomb lattice of a nanotube [20].

account the two carbon atom basis of the lattice, where  $\phi_{A,B}$  are wavefunctions that satisfy the Bloch equation:

$$\varphi_j(\vec{k}, \vec{r}) = \sum_{j,j'=A,B} C_{jj'} \phi_{j'}(\vec{k}, \vec{r}) \quad (2.3)$$

The wavefunction energies and coefficients can then be determined by solving the coefficient equation

$$[H - ES]C = 0 \quad (2.4)$$

where

$$H_{jj'} = \langle \varphi_j | H | \varphi_{j'} \rangle; \quad S_{jj'} = \langle \varphi_j | \varphi_{j'} \rangle \quad (j, j' = A, B) \quad (2.5)$$

are transfer and overlap integrals. Solving Equation 2.4 results in the 3D dispersion of graphene shown in Figure 2.2. From the dispersion, graphene is a zero-gap semiconductor with conduction and valence bands touching each other at high symmetry

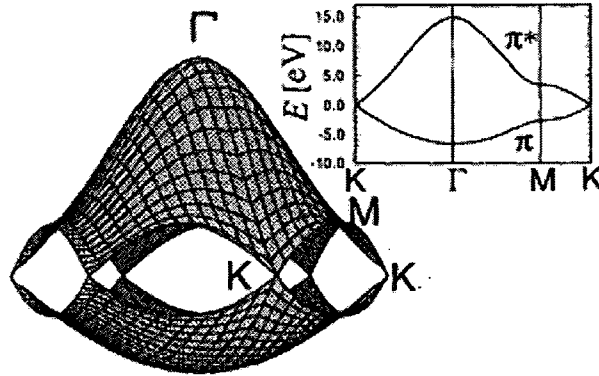


Figure 2.2 : The energy dispersion relation for 2D graphene. Conduction and valence bands are touching at K points indicating that graphene is a zero-gap semiconductor [19].

points K, K'.

The resulting approximation for 2D energy dispersion of graphene is

$$E(k_x, k_y) = \pm \gamma_0 \left\{ 1 + 4 \cos\left(\frac{\sqrt{3}k_x a}{2}\right) \cos\left(\frac{k_y a}{2}\right) + 4 \cos^2\left(\frac{k_y a}{2}\right) \right\}^{1/2} \quad (2.6)$$

where  $\gamma_0$  is the transfer integral between nearest neighbor lattice points [20].

To extend the 2D energy dispersion of graphene to SWNTs, periodic boundary conditions are imposed, where wavevectors are quantized in the circumferential direction:

$$\exp(i\vec{k} \cdot \vec{C}) = 1, \quad k_\mu = 2\pi\mu/C; \quad \mu = 0, 1, 2, \dots \quad (2.7)$$

Using the graphene dispersion relation with the quantized wavevectors, the SWNT dispersion relation becomes

$$E_\mu(k) = E_{g2D}\left(k \frac{\vec{K}_2}{|\vec{K}_2|} + \mu \vec{K}_1\right); \quad (\mu = 0, 1, \dots, N-1) \quad (2.8)$$



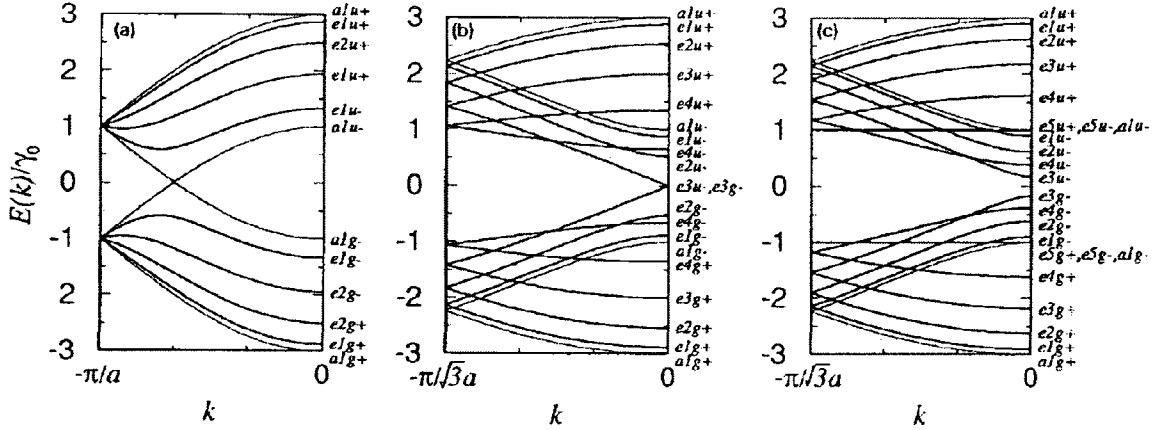


Figure 2.3 : 1D energy dispersion for (a) (5,5) armchair nanotube, (b) (9,0) zigzag nanotube, and (c) (10,0) zigzag nanotube [19, 21, 22].

The 1D energy dispersion relations for the (5,5) armchair, (9,0) zigzag, and (10,0) zigzag nanotubes are shown in Figure 2.3. If allowed  $k$  states pass through the K point in graphene, the nanotube is metallic. If the allowed  $k$  states do not pass through the K point, it is semiconducting. More specifically, from the  $(n,m)$  chirality index, a nanotube is metallic if  $n-m$  is divisible by 3.

## 2.2 Excitons in SWNTs

Coulomb interactions are enhanced in 1D systems and due to the one-dimensional nature of carbon nanotubes, optical processes as a result are strongly affected by Coulomb interactions. Because of the strong 1D confinement of electrons and holes, excitons in SWNTs have extremely large binding energies ( $> 300$  meV) compared to exciton binding energies in bulk semiconductors ( $\sim 5$  meV) [23, 24, 25, 26]. As shown in the previous section, the SWNT band structure is derived from the band structure of graphene and as such, nanotubes have equivalent conduction and valence bands in  $k$ -space around K and K' symmetry points in graphene.

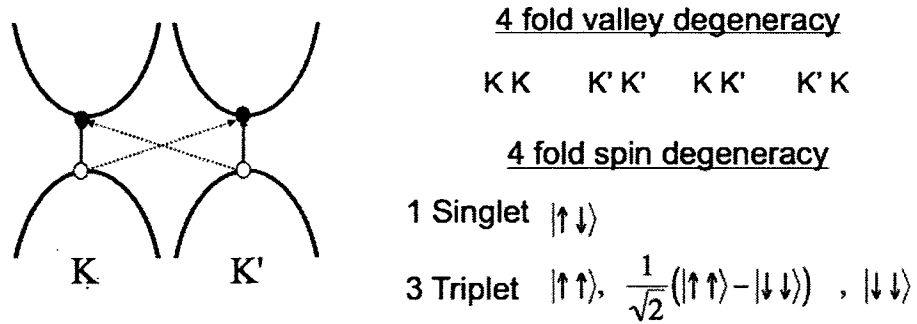


Figure 2.4 : Coulomb interactions giving rise to 16 partially degenerate exciton states in SWNTs.

Coulomb interactions between carriers in the two  $k$ -space valleys influence the energy levels and selection rules of the excitonic transitions [27]. Because the conduction and valence bands are doubly degenerate, for free electron-hole pairs, this gives four distinct but degenerate pair excitations. Shown in Figure 2.4, these four possible configurations are  $KK$ ,  $K'K'$ ,  $KK'$  and  $K'K$ .

This four-fold valley degeneracy alongside a four-fold spin degeneracy that stems from electrons and holes having spin, leads to 16 partially degenerate exciton states. More specifically, when the strongest part of the Coulomb interaction couples with spin, this gives rise to an odd parity singlet and even parity triplet states. Then, the weaker short range part of the Coulomb interaction splits and orders these singlet and triplet states further, shown in Figure 2.5. Taking into account parity and angular momentum, out of these 16 excitonic states, only one state is optically active. This optically active bright state exists within the singlet manifold and has odd parity and zero angular momentum. A lower lying optically inactive dark state with even parity and zero angular momentum exists below the optically active bright state. The separation between the dark and bright states is determined by the strength of the

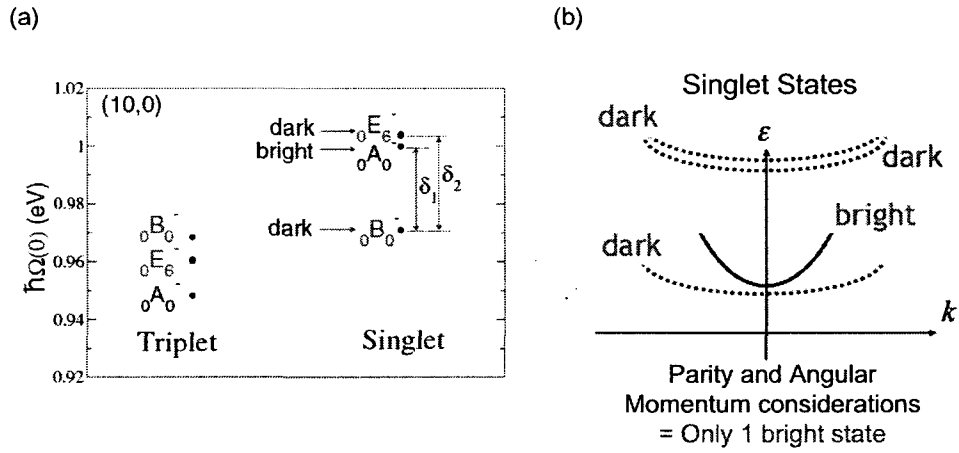


Figure 2.5 : (a) Relative energy of SWNT excitonic levels for the (10,0) nanotube [28]. (b) Singlet states: only 1 state is optically active.

electron-hole exchange interaction. Finally, above the bright singlet state, there are also two degenerate, higher energy states with nonzero angular momentum that are also optically inactive. Because nanotubes have such a unique exciton band structure with only one exciton state that is optically active and a lower lying optically inactive dark state, this greatly affects the optical properties of SWNTs, which will be further explained in later chapters.

### 2.3 Radiative decay in SWNTs

Because of energy-momentum conservation that is required for radiative decay, excitons with large center-of-mass wave vector  $K > \kappa$  cannot decay radiatively, where  $\kappa$  is the wave vector of light in the crystal with the same energy as the exciton [29, 30]. Instead, excitons with  $K < \kappa$  decay radiatively, and as radiative decay is greatly affected by not only the density of states, but also the thermal distribution of excitons, only a small fraction of thermal population decay radiatively. This can be seen in

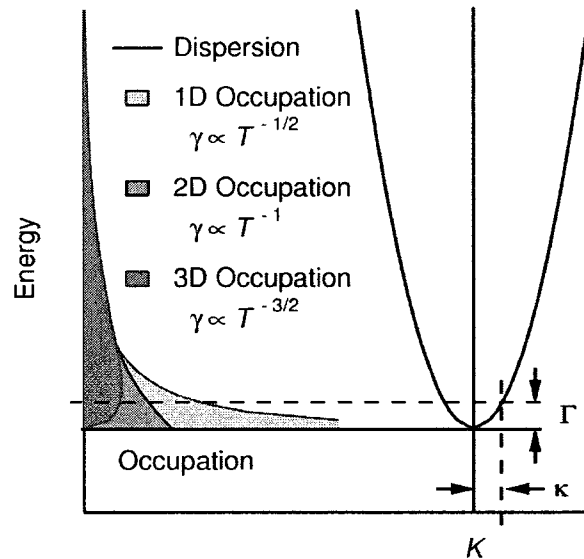


Figure 2.6 : (Left) Schematic of thermal population of excitons in systems of different dimensionality. (Right) Exciton energy dispersion. [27].

Figure 2.6, where the difference in exciton occupation near the band edge for 1, 2, and 3D systems results in varying temperature dependent radiative decay rates [27]. More specifically, the exciton energy dispersion (right) describes the optically allowed region  $|K| \leq \kappa$ .

For 1D systems, taking into account a Boltzmann distribution of excitons, Citrin calculated the radiative decay rate that scales as  $1/\sqrt{T}$  in semiconducting quantum wires, with an important assumption that the effective thermalization time of excitons is much less than the radiative lifetime [30].

Extending this to nanotubes, radiative decay rate for SWNTs is affected by a complex exciton bandstructure. In particular, the lower-lying optically-inactive dark state can trap excitons, complicating the radiative decay process. Applying the same thermalization assumptions, both Spataru *et al.* and Perebeinos *et al.* calculated the temperature dependent radiative decay rate for SWNTs [28, 31]. Figure 2.7(a) shows

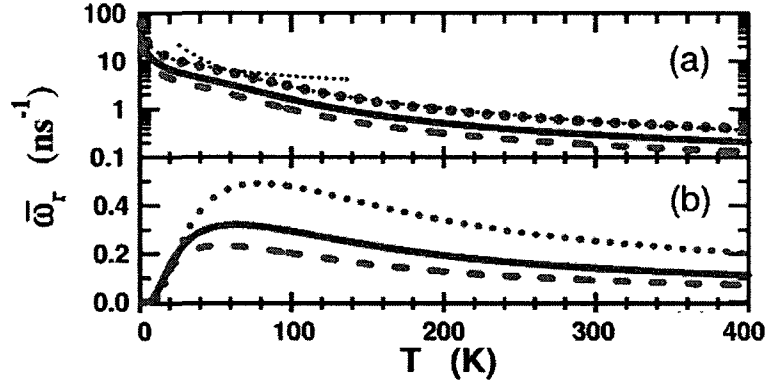


Figure 2.7 : (a) Radiative decay rate for excitons in SWNTs within the bright band only. (b) Radiative decay rate for excitons in SWNTs within the the singlet manifold. (Adapted from [31]).

the temperature dependent radiative decay rate for excitons within the bright band only. As the temperature decreases, the exciton distribution in the bright band will narrow and begin thermally populating optically active exciton states at the bottom of the band,  $|K| \leq \kappa$ . This results in an increase in the radiative decay rate with decreasing temperature.

However, considering the case of thermalization between different parity states within the singlet manifold (ie: from the optically-active (1u) bright state to the low-lying optically-inactive (1g) dark state), as temperature decreases, excitons within the bright band will populate the optically active exciton states until a critical temperature when excitons begin scattering into the dark state. This traps a large portion of the exciton population at low temperatures and causes a decrease in the radiative decay rate. This is can be seen in Figure 2.7(b).

## 2.4 SWNT band structure in magnetic field

The band structure of a nanotube is predicted to change drastically when a magnetic field is applied parallel to the nanotube axis due to the Aharonov-Bohm effect [32, 33, 34]. When a nanotube is threaded by a magnetic flux,  $\phi$ , an Aharonov-Bohm (AB) phase is generated around the nanotube circumference and modifies the circumferential boundary conditions. More specifically, the band structure is predicted to depend on  $\phi/\phi_0$  and the band gap will oscillate with a period  $\phi_0 = e/h$ , where  $e$  is the electron charge and  $h$  is Planck's constant [27]. As a result, this causes the K and K' valleys to split in energy and the band gap of a metallic (semiconducting) SWNT will open (shrink) with sufficient magnetic field.

As mentioned in Chapter 2.2, in the presence of time-reversal symmetry, the dark and bright singlet states are separated by an amount  $\Delta x$ , which is determined by the strength of the electron-hole exchange interaction. However, when a symmetry breaking perturbation such as magnetic field is applied, the K-K' degeneracy is lifted and coulomb mixing is reduced. This causes the two lowest states to be further separated by an Aharonov-Bohm induced splitting, redistributes the spectral weights between the dark and bright singlet states and increases the oscillator strength of the dark state. As a result, this will eventually yield two bright states, as shown in Figure 2.8. One important aspect to note about the symmetry breaking effect is that any excitons trapped in the lowest dark state will become optically active with the introduction of sufficient magnetic field.

## 2.5 Symmetry breaking effect on radiative decay

Using a simplified two-level model for excitons, we can extend the results for the calculated temperature dependent radiative decay rate for SWNTs (Chapter 2.3) and

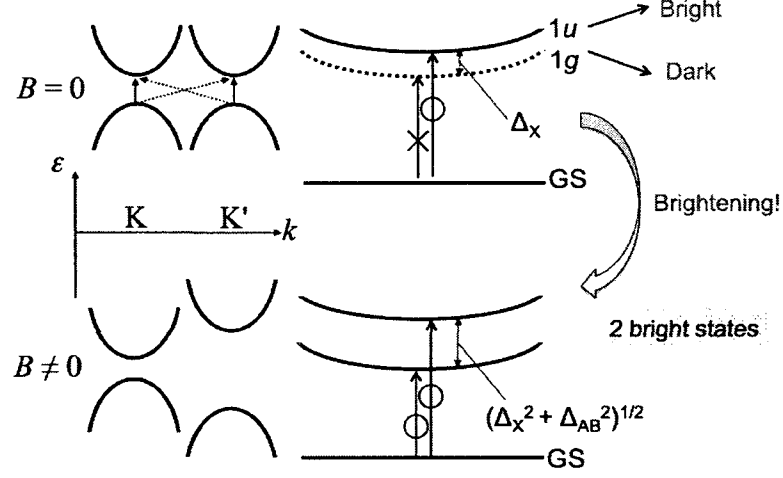


Figure 2.8 : Magnetic brightening of the dark singlet state when a symmetry breaking magnetic field is applied. (Adapted from [35]).

include the magnetic field dependence [36]. First, the relative oscillator strengths of the dark and bright excitons are given by

$$I_{\delta,\beta} = \frac{1}{2} \mp \frac{1}{2} \frac{\Delta_x}{\sqrt{\Delta_x^2 + \Delta_{AB}^2}} \quad (2.9)$$

where  $\Delta_x = \Delta_\beta - \Delta_\delta$  is the dark-bright energy splitting in zero magnetic field. The magnetic field dependence of the effective mass  $m_i^*(B)$  is

$$\frac{1}{m_\delta^*(B)} = \frac{I_\beta}{m_\delta^*(B)} + \frac{I_\delta}{m_\beta^*(B)}, \quad \frac{1}{m_\beta^*(B)} = \frac{I_\beta}{m_\beta^*(B)} + \frac{I_\delta}{m_\delta^*(B)}. \quad (2.10)$$

Using the above equations and including the Boltzmann factor,  $e^{-\frac{\sqrt{\Delta_x^2 + \Delta_{AB}^2}}{k_B T}}$ , the temperature and magnetic field dependence of the PL intensity is then

$$\gamma \propto \frac{1}{(T^2 + T_0^2)^{\frac{1}{4}}} \frac{\frac{I_\delta(B)}{I_\beta(B)} + e^{-\frac{\sqrt{\Delta_x^2 + \Delta_{AB}^2}}{k_B T}}}{\sqrt{\frac{m_\delta^*(B)}{m_\beta^*(B)} + e^{-\frac{\sqrt{\Delta_x^2 - \Delta_{AB}^2}}{k_B T}}}} \quad (2.11)$$

We will show in later sections, that this formula works well to describe the temperature dependent magnetic brightening of SWNT PL intensity, especially at high temperatures.

## 2.6 Phonons in carbon nanotubes

Just like the electronic band structure, the phonon dispersion relations for carbon nanotubes are also obtained from the phonon dispersion relations of graphene. Figure 2.9 provides a good first approximation for the 2D phonon dispersion relation of graphite. Noting the  $\Gamma$  point in the graph, there are three phonon dispersion branches corresponding to acoustic modes that originate from the  $\Gamma$ -point of the Brillouin zone in graphene with  $\omega=0$ . In order of increasing intensity, there is the out-of-plane mode, the in-plane tangential mode, and an in-plane radial mode [19]. The three higher modes are optical modes that correspond to one non-degenerate out-of-plane mode and two degenerate in-plane modes.

The zone folding method can then be used to determine the phonon dispersion relation for nanotubes from 2D graphene phonon dispersion curves,  $\omega_{2D}^m(\vec{k})$ , where  $m = 1, \dots, 6$  for the 3 acoustic and 3 optical modes and  $\vec{k}$  is the vector in the layer plane.

As shown before for determining the electronic band structure of SWNTs, the phonon wave vector will also become discrete in the circumferential direction due to the periodic boundary conditions defined by the chiral vector,  $\vec{C}_h$ . Therefore, using zone folding [19], the 1D phonon dispersion for SWNTs,  $\omega_{1D}^{m\mu}(k)$ , becomes:

$$\omega_{1D}^{m\mu}(k) = \omega_{2D}^m(k) \left( k \frac{\vec{K}_2}{|\vec{K}_2|} + \mu \vec{K}_1 \right) \quad (2.12)$$

where  $m = 1, \dots, 6$ ,  $\mu = 0, \dots, N - 1$ , and  $-\frac{\pi}{T} < k \leq \frac{\pi}{T}$ . Moreover,  $\vec{K}_2$  is the



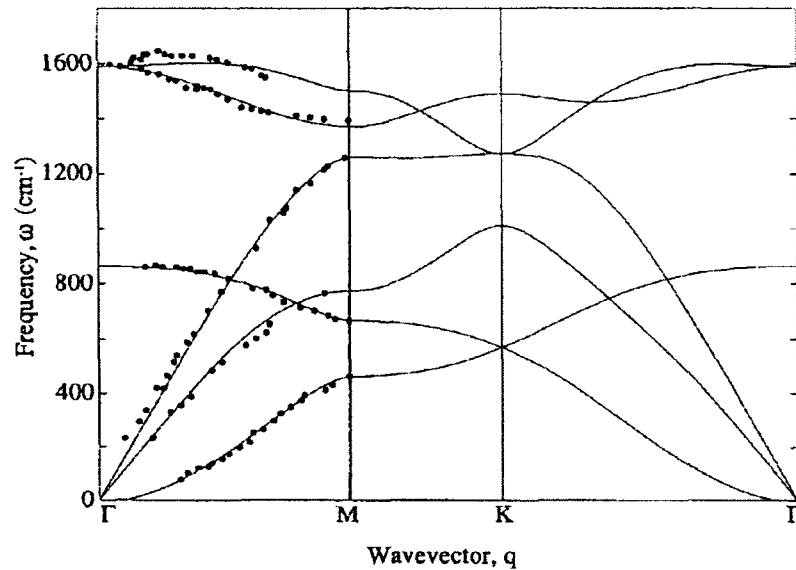


Figure 2.9 : The phonon dispersion relation for graphite plotted along the high-symmetry in-plane directions [37].

reciprocal lattice vector along the nanotube axis,  $\vec{K}_1$  is the reciprocal lattice vector in the circumferential direction, and  $\vec{T}$  is the magnitude of the translation vector,  $\vec{T}$  in Figure 2.1.

Figure 2.10 shows the calculated phonon dispersion and low energy phonon dispersion for the (10,10) armchair nanotube. In particular, from the calculated low-energy phonon dispersion, there are four acoustic modes: two degenerate transverse acoustic modes, one longitudinal acoustic mode, and one "twist" acoustic mode. All other higher energy phonons are optical phonons. Figure 2.11 shows the radial breathing mode optical phonon that came about from its corresponding out-of-plane tangential acoustic mode with  $\vec{k}=0$  in graphene. We will show in later sections some optical measurements investigating the RBM in SWNTs.

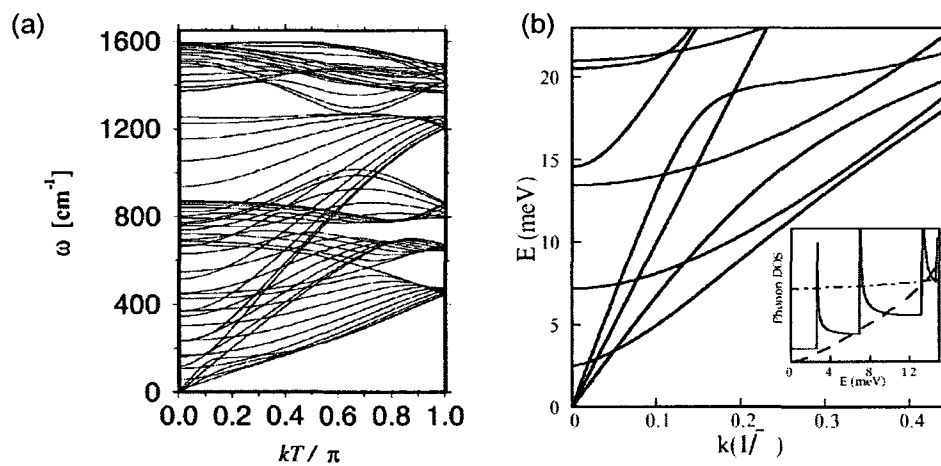


Figure 2.10 : (a) Calculated phonon dispersion for (10,10) armchair nanotube. (b) Low-energy phonon dispersion curves for the (10,10) armchair nanotube [20].

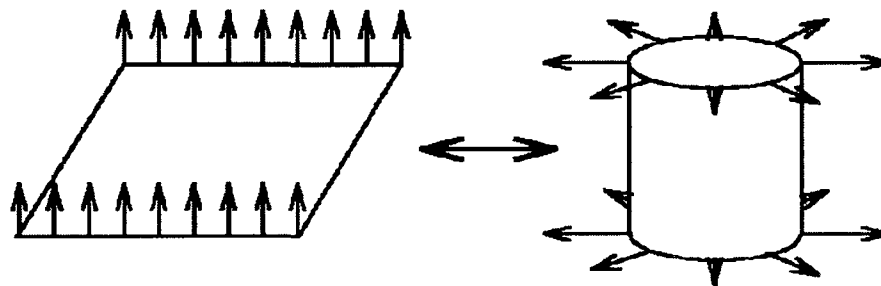


Figure 2.11 : (Left) Out-of-plane tangential acoustic mode in graphene becomes (Right) the radial breathing mode optical phonon for SWNTs [20].

## Chapter 3

### Magnetic Brightening of Dark Excitons

In understanding the radiative and non-radiative decay mechanisms and the role of dark excitons on the quantum efficiency in SWNTs, much focus has been placed on understanding the influence of temperature and magnetic field on SWNT photoluminescence (PL) intensity. Our previous experimental studies investigating the temperature dependence of SWNT ensembles at high magnetic fields have uncovered a magnetic-field-induced increase by a factor of 6 of the PL intensity at low temperatures down to 1.5 K, while our recent micro-PL spectroscopy study of individual SWNTs in magnetic fields up to 5 T has shown that there are significant environmental effects that affect the excitonic fine structure [36, 38].

Although progress has been made in understanding the role of dark excitons on the radiative decay process, there are still many questions left unanswered. It has been suggested that the role of defects or disorder also have a symmetry-breaking role similar to magnetic fields, causing magnetic brightening at low temperatures. Additionally, theory suggests that at low temperatures, when the thermal energy becomes smaller than the dark-bright splitting energy, all excitons will populate the lowest dark excitonic state, resulting in the complete disappearance of PL. Driven by these questions, our current work focuses on mK-temperature-dependent studies well below 1.5 K, to make the thermal energy much smaller than the dark-bright splitting and to understand exciton dynamics at very low temperatures.

Utilizing a unique dilution refrigerator and superconducting magnet system at

Tohoku University that offers the ability to perform magneto-optical studies at mK temperatures, we measured temperature dependent magnetic brightening of the photoluminescence of DNA-wrapped CoMoCat SWNTs dispersed in a polyacrylic acid PAA matrix thin films. Measuring the magnetic field dependence up to 5 T at 50 mK and 4.3 K with excitation energy of 670 nm, we obtained an unexpected PL intensity for 50 mK at zero-field that is comparable to the zero-field intensity at 4.3 K. Additionally, comparing the magnitude of magnetic brightening, both 50 mK and 4.3 K exhibit the same increase in magnetic brightening. Such results are contrary to current theory, as we expected zero PL at mK temperatures, with the largest increase in magnetic brightening at very low temperatures. Such results imply novel explanations such as a non-thermal distribution of excitons at low temperatures, defect-induced partial brightening of the dark state, and the inaccuracy of the Boltzmann distribution to describe the relative populations of the bright and dark exciton bands.

### 3.1 Previous magnetic brightening measurements

Zaric *et al.* performed near-infrared magneto-optical spectroscopy of SWNTs and measured two absorption peaks with equal strength at high magnetic fields [35, 14]. As shown in Figure 3.1(a), they discovered that when the magnetic field is parallel to the nanotube axis, the peak separation of the absorption peak at zero magnetic field into two peaks at high magnetic field ( $>55$  T) is determined by the Aharonov-Bohm phase that breaks the time-reversal symmetry and lifts the valley degeneracy of SWNTs. This is further supported by the absence of any peak splitting when the magnetic field is perpendicular to the tube axis (Figure 3.1(b)).

Shaver *et al.* furthered the above magneto-optical measurements by measuring temperature dependent magneto-PL of SWNT films. As shown in Figure 3.2, they showed that symmetry breaking magnetic field can increase the PL quantum yield of

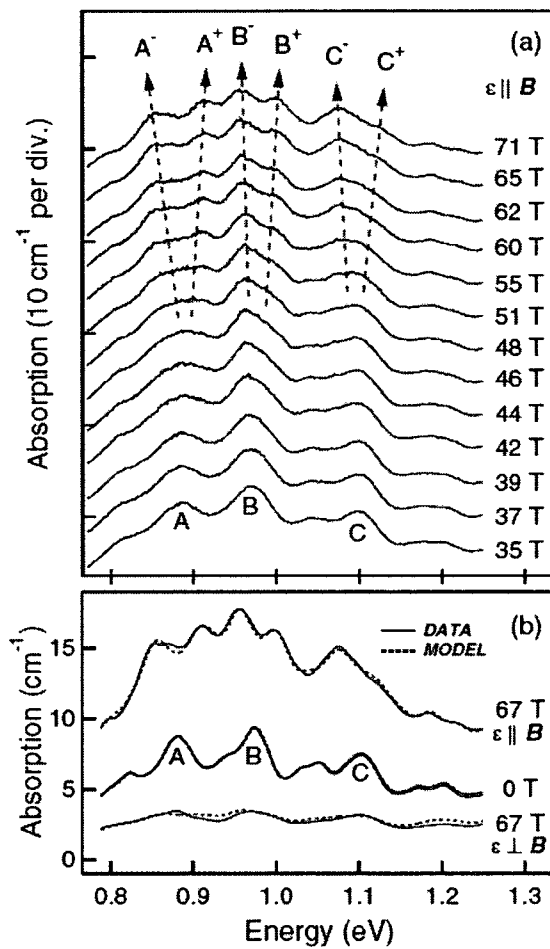


Figure 3.1 : Near band-edge absorption in semiconducting SWNTs in high magnetic fields for (a) polarization parallel to B and (b) both parallel and perpendicular to B [35].

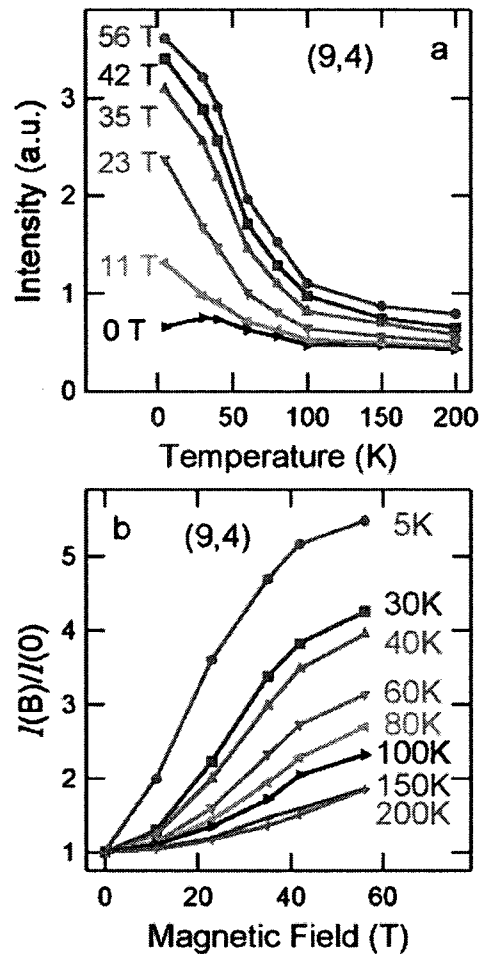


Figure 3.2 : Temperature dependence of magnetic brightening as a function of (a) temperature (b) magnetic field [36].

a SWNT by a factor of 6 at low temperatures. Their results were the first clear experimental observation of dark excitons 5-10 meV below the bright excitons [36]. The role of the dark exciton on PL intensity can also be further verified by Figure 3.2(a), where the PL intensity decreases below  $\sim 25$  K at 0 T, as is expected from Chapter 2.3. They were also able to successfully fit their results to Equation (2.11) at high temperatures.

All of the above measurements were made using ensemble samples, where the optical measurements investigated many nanotubes. As a result, this can cause broadening of absorption and PL features and the existence of dark excitons could only be inferred from the T and B dependence of the PL intensity. However, Srivastava *et al.* reported direct observation of the spin-singlet dark exciton in individual SWNTs by measuring low-temperature micro-magneto-PL spectroscopy [38]. As shown in Figure 3.3, there is the appearance of the dark exciton peak at a lower energy when a magnetic field is applied to the single nanotube. The dark exciton peak grows with field at the expense of the bright exciton peak, eventually becoming dominant at fields  $>3$  T. In Figure 3.3(b), they also verify the absence of any magnetic brightening of the dark exciton peak when the magnetic field is applied perpendicular to the single nanotube. They observed this behavior for more than 50 nanotubes, and directly measured a dark-bright splitting of 1-4 meV for tube diameters ranging between 1.0-1.3 nm.

## 3.2 Experimental methods

### 3.2.1 Dilution refrigeration

A dilution refrigerator is a cryogenic device that uses a mixture of He-3 and He-4 to cool to temperatures in the milliKelvin regime. To describe the dilution refrigera-

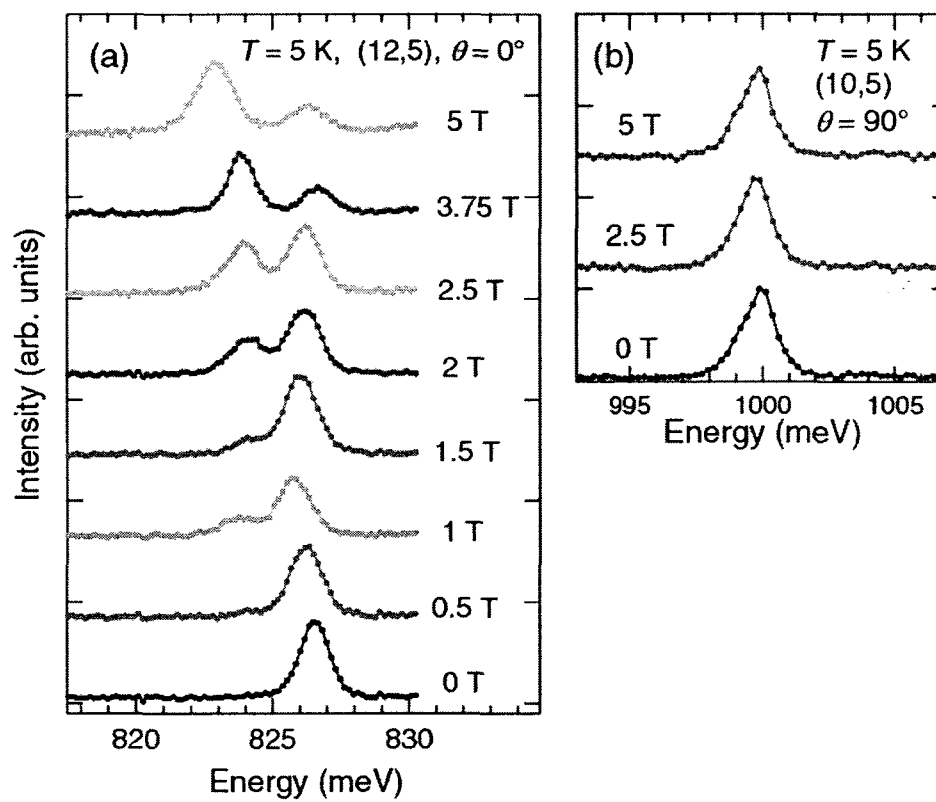


Figure 3.3 : Micro-magneto PL of a single nanotube when the magnetic field is (a) parallel (b) perpendicular to the nanotube axis [38].



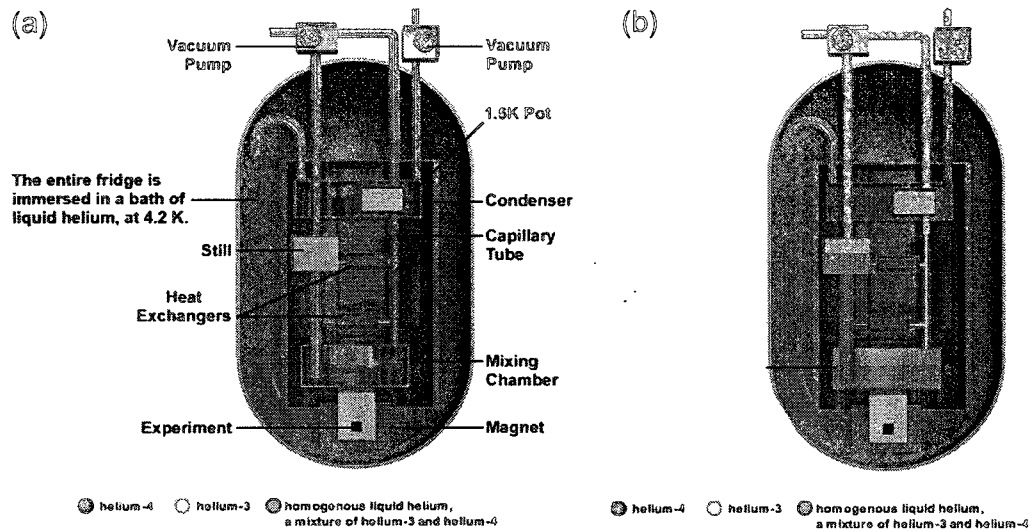


Figure 3.4 : (a) Dilution refrigerator before refrigeration cycle. (b) Dilution refrigerator during refrigeration cycle [39].

tion process, a detailed animation and guide from the National High Magnetic Field Laboratory website was referenced and summarized below [39].

Figure 3.4 shows a typical diagram of a dilution refrigerator. Firstly, liquid helium is used to immerse the entire fridge in a bath with temperature at 4.2 K before some of that helium is siphoned off into the 1.5 K pot. Using the vacuum pump (right), the vapor pressure is lowered in the pot and some of the liquid helium in the pot evaporates. This lowers the temperature of the pot to 1.5 K.

Next, an exact mixture of He-3/He-4 is passed through the pipe attached to the vacuum pump (left) and through the 1.5 K pot. Because the liquid helium in the 1.5 K pot is being vaporized, this lowers the temperature of the He-3/He-4 gas in the pipe. The cooled gas mixture condenses into the still and mixing chamber as a homogenous mixture of liquid helium. The vacuum pump (left) then lowers the vapor pressure in the still, causing evaporation and cooling the remaining liquid in the still.

As He-3 evaporates faster than He-4, most of the evaporation is from He-3, leaving behind liquid He-4 in the still.

Now, the refrigeration cycle begins. The He-3 gas will pass through a cold trap that acts to purify the gas. It will then be sent into the condenser within the 1.5 K pot and reliquefies. This reliquefaction process is maintained by a very narrow capillary tube located beneath the condenser that provides flow impedance to maintain the pressure. Next, the He-3 passes through heat exchangers to cool it down to the target temperature.

As the mixing chamber is also connected to the still, the liquid He-3 coming from the condenser is added to the mostly liquid He-4 that was in the mixing chamber at the beginning of the refrigeration cycle. At temperatures lower than 800 mK, the He-3/He-4 mixture will phase separate, where the top layer contains mostly He-3 and the bottom mixture contains mostly He-4 and some He-3. Because He-3 atoms have been vaporizing out of the still, which lowers the concentration of He-3 in the still. As a result, He-3 from the bottom layer of the mixing chamber will be driven up into the still via osmosis. Finally, He-3 from the top layer will cross over to the bottom layer. This process will cycle and maintain mKelvin temperature cooling while in operation.

For our measurements at Tohoku University, we used an Oxford Kelvinox MX50 dilution refrigerator, as shown in Figure 3.5. This model provides for base temperature of  $< 25$  mK and a maximum temperature of 1 K. With this system, we performed temperature dependent measurements down to 50 mK.

### 3.2.2 mKelvin photoluminescence spectroscopy

Photoluminescence (PL) spectroscopy is a nondestructive method to probe the electronic band structure of materials. Photoluminescence is the re-emission of photons

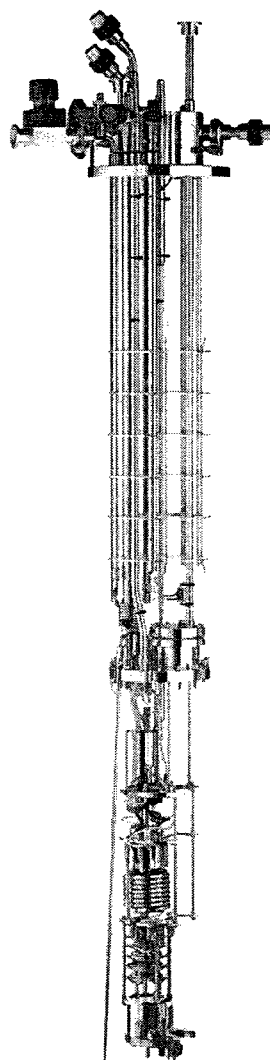


Figure 3.5 : Oxford Kelvinox MX50 Dilution Refrigerator [40].

after absorbing a photon of higher energy. More specifically, when exciting a material with photons at energies higher than its band gap, electron-hole pairs or excitons are created, which then relax back to the ground state by emitting photons [41]. For our PL measurements, in particular, we excite our nanotube sample with energy corresponding to the  $E_{22}$  conduction band of the (8,3) nanotube. This corresponds to excitation wavelength of 670 nm. Once carriers are excited to  $E_{22}$ , they will then relax nonradiatively to the  $E_{11}$  conduction band before returning to the ground state and emitting PL. The emitted PL is at a lower energy than the excitation energy and can be detected with IR detection sources.

Combining PL spectroscopy with dilution refrigeration and a superconducting magnet, we can investigate magnetic field dependence of mK PL of the (8,3) nanotube. Because we are performing ultra-cold measurements, it is important to investigate a nanotube film sample that can withstand freezing temperatures without damage to the film. Therefore, our sample of choice was DNA-wrapped CoMoCAT SWNTs in a polyacrylic acid matrix.

The experimental setup for our measurements is shown in Figure 3.6. Using a laser diode (LD) with center wavelength of 670 nm, we first use a short pass filter (700 nm short pass) to remove any higher order frequencies of light in the laser excitation. As we will be detecting PL in the IR regime, it is important that the detect signal does not include any source from the laser. Next, the laser is reflected off a pellicle beamsplitter, where it is reflected into an objective lens that is coupled to a multimode fiber. This fiber is then coupled to a single-mode fiber inside the dilution refrigerator that is inside the superconducting magnet (Oxford Instruments Solenoid Superconducting Magnet). The sample is attached to the cold finger of the dilution refrigerator, as shown in Figure 3.7. Not only does this provide strong thermal and mechanical contact of the sample to the cold finger, ensuring that the sample can reach

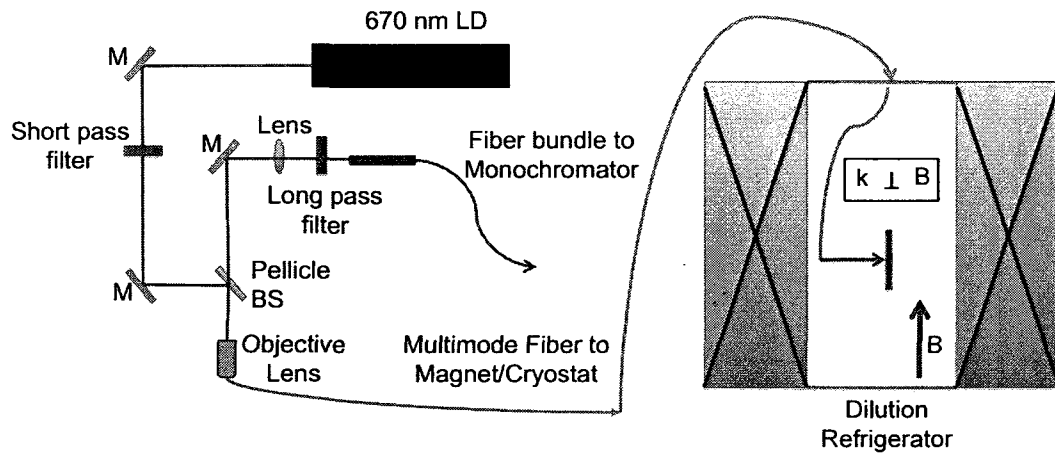


Figure 3.6 : Magnetic field dependent mK PL experimental configuration. LD: laser diode, M: mirror, BS: beamsplitter.

mK temperatures, it also allows excitation of the sample in Voigt geometry. More specifically, this means the laser polarization is perpendicular to the magnetic field polarization in the sample. As the nanotubes in the sample is randomly oriented, only the nanotubes aligned with the same orientation as the magnetic field polarization will have the greatest nanotube-threading magnetic flux. It will be these tubes that have the greatest Aharonov-Bohm induced splitting and magnetic brightening.

Not only does the single-mode fiber excite the sample with the LD, it is also used to collect the PL from the sample. The PL returns through both fibers and back through the objective lens, where it continues through the pellicle beamsplitter and a long pass filter (850 nm long-pass). This long pass filter ensures that only PL transmits to the detector and removes any stray LD in the path of the PL. The transmitted PL is then fiber coupled to the monochromator (Horiba Scientific FHR 1000) and Si:CCD detector (Horiba Scientific Symphony 1024x256 BIDD type) for detection and collection of mK PL spectrum. The LD excitation power was  $\sim 20 \mu\text{W}$  and the total collection time was 50 minutes.

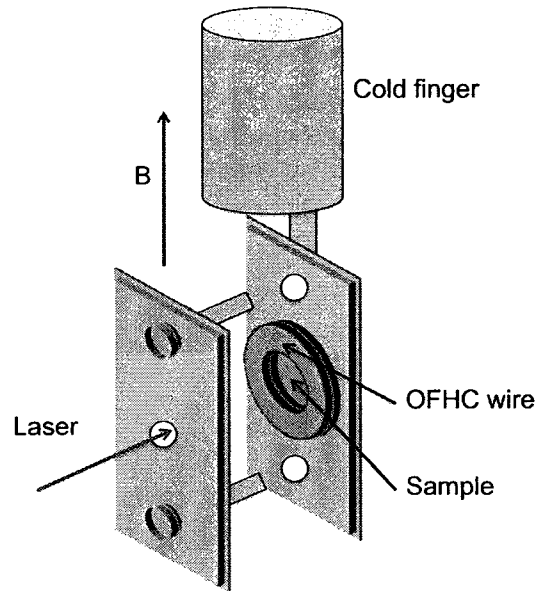
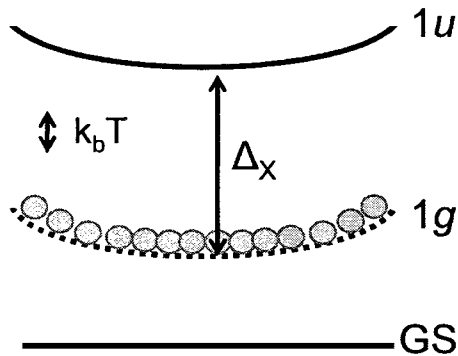


Figure 3.7 : Diagram of cold finger with nanotube sample attached. OFHC: oxide-free, high conductivity copper wire.

### 3.3 Experimental Results

We performed temperature-dependent magnetic brightening of DNA-wrapped CoMo-CAT SWNT thin films at Tohoku University, utilizing their dilution refrigerator and superconducting magnet system. We began by investigating zero-field PL at 50 mK and 4.3 K and our results are shown in Figure 3.9. It is important to notice that the PL for 50 mK is comparable to 4.3 K, which is contrary to what is expected from current theory. As reviewed in Chapter 2.3 (Radiative decay in SWNTs), current theory suggests that as the temperature approaches 0 T, all excitons should occupy the dark state.

This can also be explained quantitatively by comparing the dark-bright splitting of the (8,3) to the thermal energy at 50 mK. Previous experiments have calculated a zero-field dark bright splitting of about  $\Delta_x = 5$  meV for the (8,3) nanotube and we



All excitons should  
occupy the dark state

Figure 3.8 : Current Theory: Lowest lying bright and dark singlet states. At 50 mK, the thermal energy is much smaller than the dark-bright splitting.

calculate the thermal energy at 50 mK to be  $k_b T = 5\mu\text{eV}$  [31, 42, 43] . As such, the thermal energy is three orders of magnitude smaller than the dark-bright splitting. Furthermore, we can calculate the relative population of excitons between the bright and dark state by calculating the Boltzmann factor:

$$\frac{N_b}{N_d} \propto e^{-\frac{\sqrt{\Delta_x^2 + \Delta_{AB}^2}}{k_b T}} = 10^{-534} \cong 0 \quad (3.1)$$

This population ratio of zero between the bright and dark state implies that the dark state is completely occupied. Therefore, at 50 mK and zero magnetic field, current theory predict zero PL because all excitons should occupy the dark state (Figure 3.8). However, our non-zero PL at 50 mK is surprising and contradicts with current theory.

Continuing with our measurements, we proceed to measure magnetic brightening of the (8,3) nanotube at 50 mK and 4.3 K by sweeping the magnetic field from 0 T-

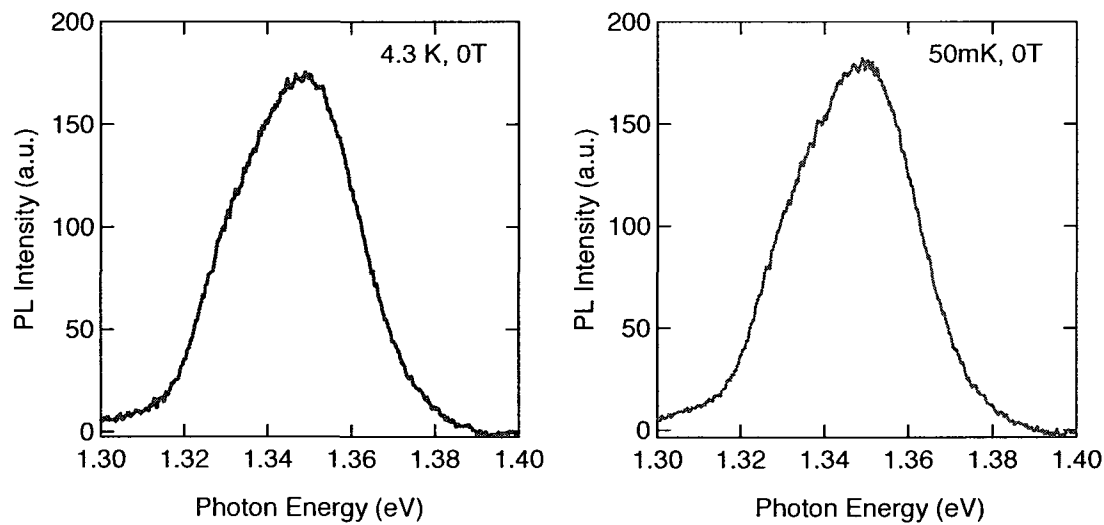


Figure 3.9 : Zero-field PL for (8,3) at 4.3 K and 50 mK. 50 mK PL is comparable to 4.3 K, unexpected with current theory.

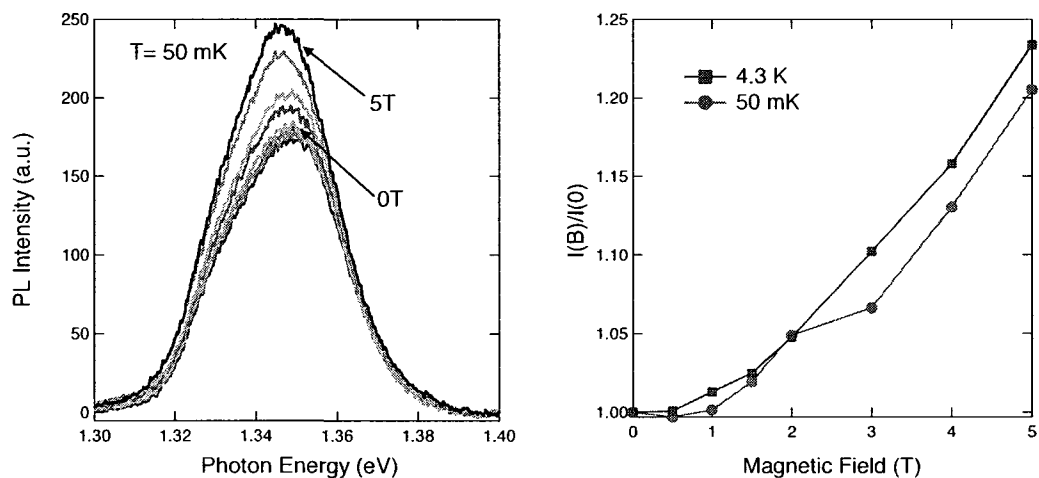


Figure 3.10 : (Left) Magnetic brightening of the PL spectrum for the (8,3) nanotube at 50 mK. (Right) Magnetic brightening for 50 mK compared with 4.3 K.



5 T. As shown in Figure 3.10, we see an increase of  $\sim 20\%$  in PL intensity and the expected red-shifting with increasing magnetic field. We also note that the magnetic brightening at 50 mK is comparable to 4.3 K, contradicting with current theory that suggests that at mK temperatures, the PL magnetic brightening should be very large compared to temperatures of a few kelvin. In particular, using Eq. 2.3 from current theory, we can calculate the expected PL intensity for 50 mK at 5 T:

$$\frac{\gamma(5T)}{\gamma(0T)} \cong 10^{15} \quad (3.2)$$

It is obvious that our magnetic brightening at 5 T is not  $10^{15}$  and it is therefore clear that the current theory is inadequate to describe our mK PL and magnetic brightening.

### 3.4 Analysis and Discussion

As our low temperature results contradict with current theory, we will consider first the possibility that disorder plays a role in partially brightening the dark state at zero field. Disorder is any non-magnetic field, symmetry breaking perturbation and from Eq. 2.3 from current theory, disorder exists in the Aharonov-Bohm induced splitting:

$$\Delta_{AB} = \frac{2\gamma LB}{\phi_0} + \Delta_{dis} \quad (3.3)$$

Examples of disorder can be any defects or impurities in the nanotube sample. More importantly, disorder can cause finite brightening of the dark state without any added magnetic field. Fitting our 50 mK magnetic brightening data to Eq. 2.3 and including various amounts of disorder, Figure 3.11 shows the results of our fitting.

It is important to first note that the theory is linear, while qualitatively our 50 mK brightening data is superlinear. It is clear that the current theory does not account for the nonlinearity of our data. However, at 50 mK, even though the fit to the entire

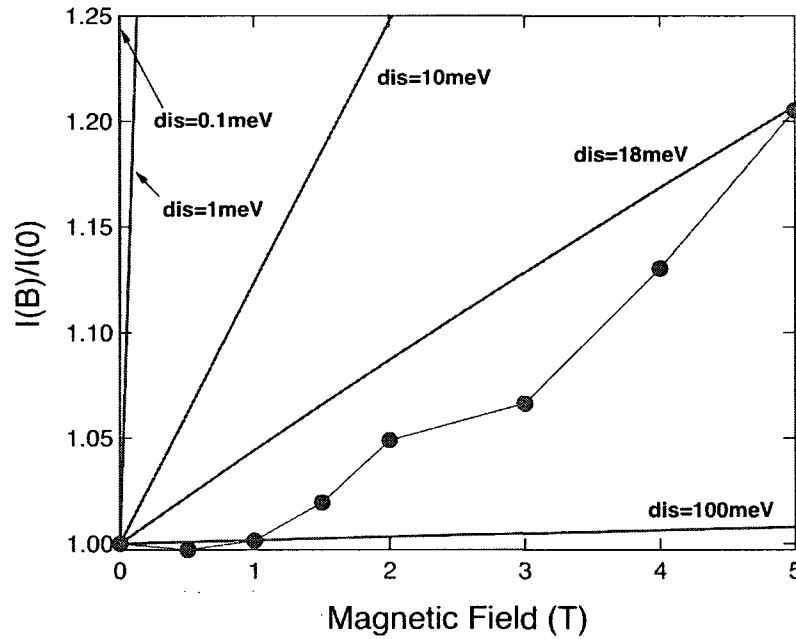


Figure 3.11 : Fitting of current theory with various amounts of disorder to 50 mK magnetic brightening.

data is poor, the 20 % magnetic brightening is consistent with 18 meV of disorder. However, not only is this value inconsistent with previous work , 18 meV of disorder is equivalent to applying a magnetic field of about 18 T, which is unreasonable with measurements limited to 5 T. Our results indicate that disorder cannot explain our PL intensity.

Considering the possibility that acoustic phonons are inefficient at thermalizing excitons and there is in fact a non-thermal distribution of excitons, lets us replace the Boltzmann factor with a constant that we represent here as R and determine the population ratio at 50 mK. This now changes Eq. 2.3 to

$$\gamma \propto \frac{1}{(T^2 + T_0^2)^{\frac{1}{4}}} \frac{\frac{I_\delta(B)}{I_H(B)} + R}{\sqrt{\frac{m_\delta^*(B)}{m_\beta^*(B)} + R}} \quad (3.4)$$

Figure 3.12(a) shows the fitting of our 50 mK magnetic brightening to Equation 3.4. We first note how well this function actually fits our mK data, more accurately following the nonlinearity of the data. Also, the results of our fit produces  $R = 0.45$ . As shown in Figure 3.12(b), this finite population ratio means that 45 % of the entire exciton population is still in the upper state. This is unlike the linear fit of the current theory, where all excitons are thermalized and  $R$  is zero. This improvement to the fit, more accurately describes our data and therefore, we can confidently say that at low temperatures, our PL data is affected by a non-thermal distribution of excitons.

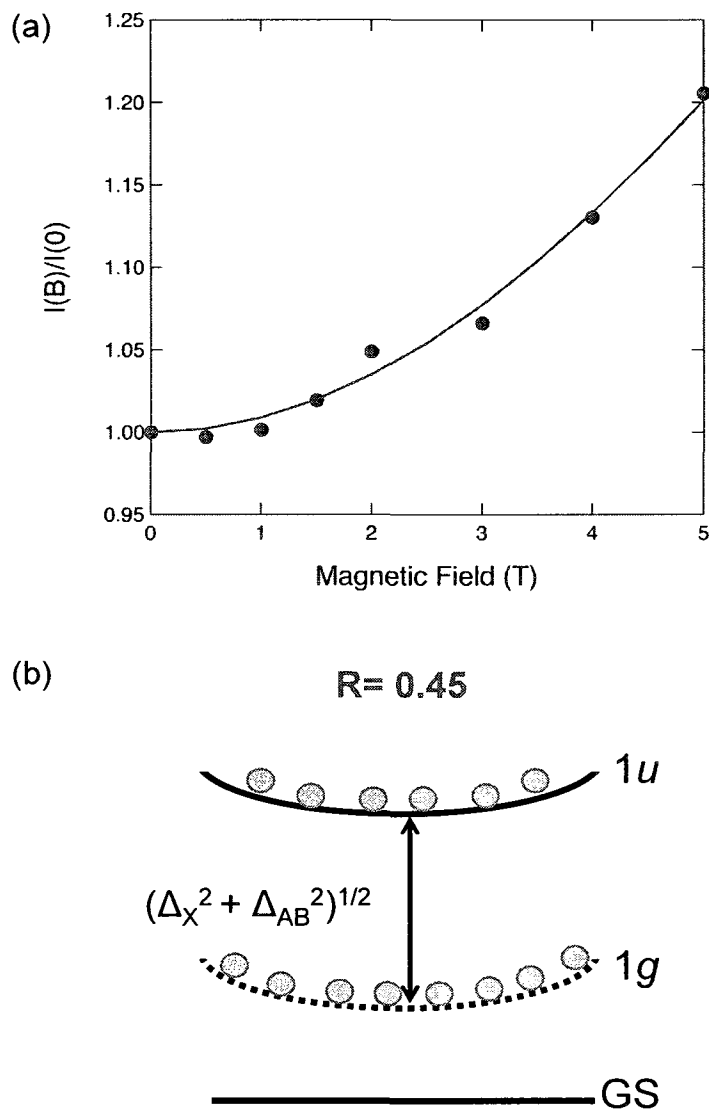


Figure 3.12 : (a) Fitting of Equation 3.4 to the 50 mK magnetic brightening. (b) Fit results produce a value of 0.45 for  $R$ , indicating that 45% of the entire exciton population is still in the bright state at 50 mK.

## Chapter 4

# Polarization Dependent Coherent Phonon Spectroscopy

Coherent phonon (CP) spectroscopy is an ultrafast pump-probe technique that rivals resonant Raman spectroscopy and although both techniques provide information about electron-phonon coupling, CP spectroscopy avoids the common disadvantages of Raman spectroscopy that include detection of Rayleigh scattering and photoluminescence and the broadening and blending of peak features. Such advantages are useful when investigating single-walled carbon nanotubes (SWNTs), where a large majority of samples include ensembles dispersed in various environments and their optical properties are obscured by the collection of varying species of nanotubes.

Recent CP studies on SWNTs have produced direct observation of CP oscillations of both the radial breathing mode (RBM) and G-band phonons, in addition to their phase information and dephasing times [44, 45, 46, 47, 48]. Furthermore, when pulse-shaping techniques are combined with CP spectroscopy, predesigned trains of femtosecond pulses selectively excite RBM CPs of a specific chirality, avoiding inhomogeneous broadening from the ensemble [49]. However, it is important to note that previous CP studies investigated randomly aligned SWNT samples and as the quasi-1D nature of SWNTs leads to optical anisotropy that is dominant in the polarization dependence of PL, absorption, and Raman scattering, CP studies on aligned SWNTs are necessary.

Here we present the first polarization study of CPs in highly aligned SWNT thin

films and found a very strong polarization anisotropy of the RBM as a function of angle. In particular, we observed a complete quenching of the RBM when optical polarization is perpendicular to the tubes. Fitting our results, we also calculated the pneumatic order parameter,  $S$ , and determined the order of alignment of our sample.

## 4.1 Coherent Phonons

In general, the phonon modes of vibrations are at random phases from each other throughout the crystal lattice. However, if the atoms in the lattice experience a driving force, then the phonons can become in-phase, becoming coherent phonons. These phonons can then interfere with each other, much like normal modes in wave mechanics.

Coherent phonons can be observed by exciting the phonons with a ultrafast laser pulse that is shorter than the duration of the phonon oscillation period. The generated coherent phonons will stay in-phase for a short period of time, their lifetime is dictated by dephasing mechanisms that are derived from many sources, ie: anharmonic decoupling, temperature, crystalline defects, and electron-phonon coupling.

The classical equation of motion for a driven harmonic oscillator is used to describe coherent phonon motion for a small nuclear displacement  $Q$  [50, 51, 52, 53]:

$$\mu \left[ \frac{\partial^2 Q(t)}{\partial t^2} + 2\gamma \frac{\partial Q(t)}{\partial t} + \omega_0^2 Q(t) \right] = F(t) \quad (4.1)$$

with the reduce lattice mass  $\mu$ , the damping  $\gamma$ , and the frequency  $\omega$ . More specifically, there are two classifications of coherent phonon generation: impulsive and displacive. Figure 4.1 displays both types of generation mechanisms.

For the impulsive excitation, the mechanism can be described via Impulsive Stimulated Raman Scattering (ISRS). ISRS can occur for both nonresonant and resonant

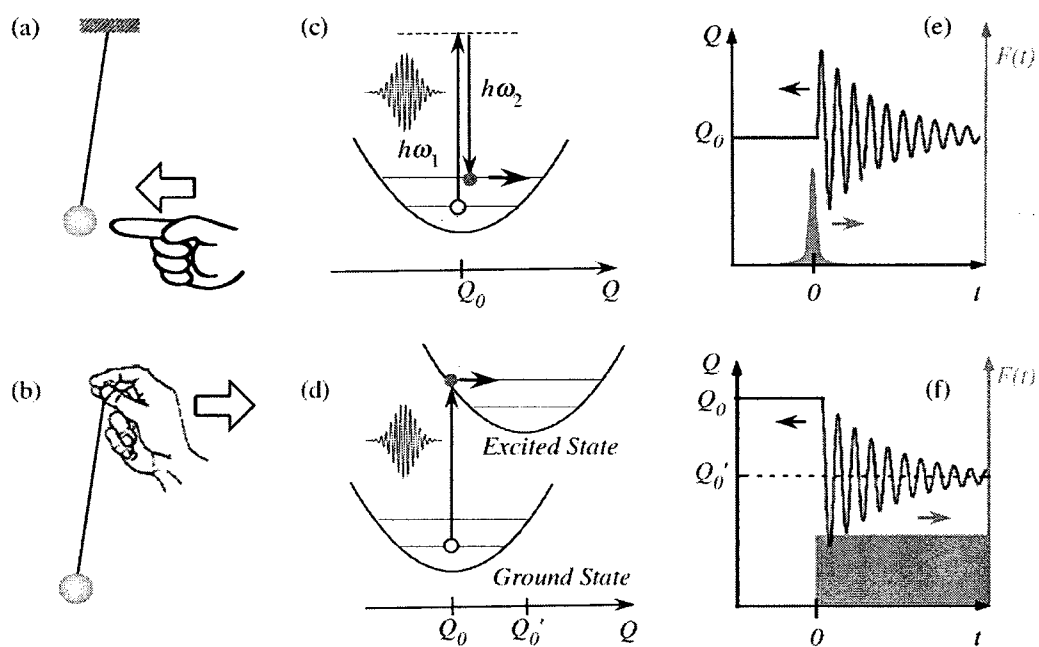


Figure 4.1 : (a), (c), (e) ISRS generation mechanism. (b), (d), (f) DECP generation mechanism [50].

cases, where the resonant case enhances Raman scattering cross sections and the amplitude of ISRS generated coherent phonons [50]. The key requirements for ISRS are Raman active modes and a broadband pulse with a pulse duration shorter than the phonon period. The broadband optical pulse can provide many possibilities for combinations of two photons with a difference that matches the vibrational energy, which then provides the impulsive driving force that initiates coherent nuclear motion on the ground state [50]. The driving force is defined by the Raman polarizability [51, 53]:

$$F(t) = \frac{1}{2} \left( \frac{\partial \alpha}{\partial Q} \right)_{kl} E_k E_l \quad (4.2)$$

The resulting nuclear oscillation follows a sine function. The  $\delta$ -function-like driving force of ISRS is analogous to giving a kick to the weight of a pendulum and changing its kinetic energy [50].

For the second case, displacive excitation generates coherent oscillations in the excited state when there is a sudden shift in potential energy surface, as shown in Figure 4.1. The key requirements are that electron-phonon coupling can shift the potential energy surface by electronic excitation and that the broadband pulse has a pulse duration that is shorter than the phonon period. The resulting nuclear oscillation follows a cosine function. The step-function-like driving force via a potential shift in the excited state of DECP is analogous to changing the potential energy of a pendulum by quickly translating its suspension point [50].

Figure 4.2 shows the coherent phonon oscillations of Sb and Bi from their transient pump-induced reflectivity change. There are two components of the signal: coherent nuclear motion from the two Raman active  $A_{1g}$  and the  $E_g$  symmetry modes and a non-oscillatory component from the modification of the electronic and lattice temperatures [50, 54, 55]. Furthermore, as shown in Figure 4.3, where the open circles are the oscillatory component of the reflectivity changes of Bi, the solid line is a fit



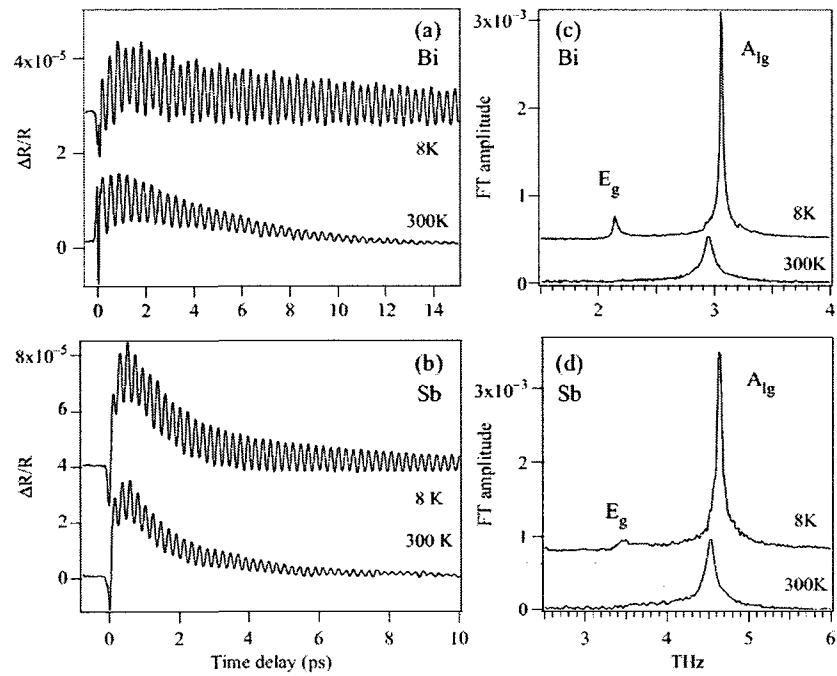


Figure 4.2 : Transient reflectivity measurements and corresponding FT spectrum for (a) bismuth and (b) antimony [50, 54, 55].

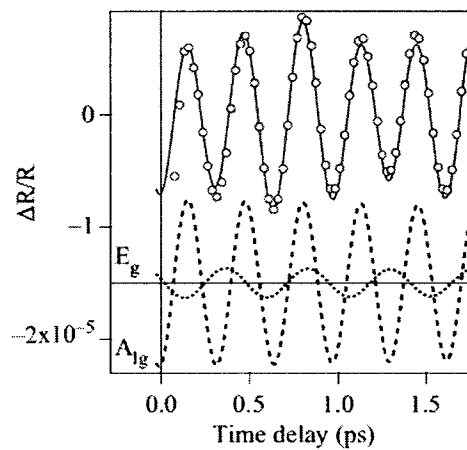


Figure 4.3 : Oscillatory part of the reflectivity in Bi at 8 K and fit to double damped harmonic function [50, 54, 55].

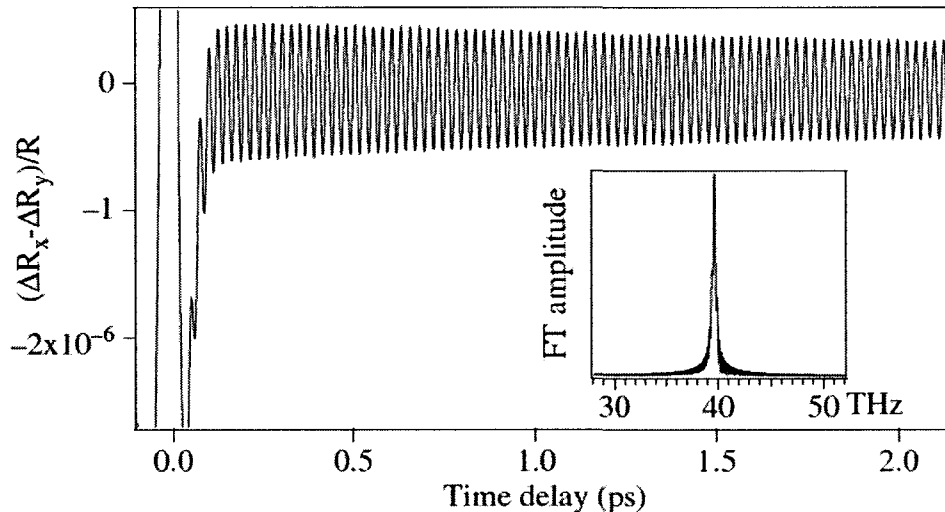


Figure 4.4 : Transient reflectivity change and FT spectrum for (001) surface of single crystal type IIa diamond [50, 56].

to a double damped harmonic function, the broken and dotted curves indicate that the  $A_{1g}$  and the  $E_g$  components are cosine and sine functions, respectively. Moreover, this implies a displacive generation for  $A_{1g}$  and a ISRS generation for  $E_g$ .

Figure 4.4 shows another example of coherent oscillations with the transient reflectivity change of the (001) surface of single crystal type IIa diamond. The time-domain data shows a dephasing time of  $0.145 \text{ ps}^{-1}$  and the FT spectrum shows a narrow optical phonon peak at 40 THz.

## 4.2 Previous CP spectroscopy measurements

Lim *et al.* generated and detected coherent phonon oscillations in SWNTs using ultrashort laser pulses with a pulse width  $\sim 50\text{fs}$ . Using pump-probe spectroscopy, coherent phonons in individualized SWNTs were observed that corresponded to the radial breathing mode (RBM) and found that these RBM CPs exactly correspond

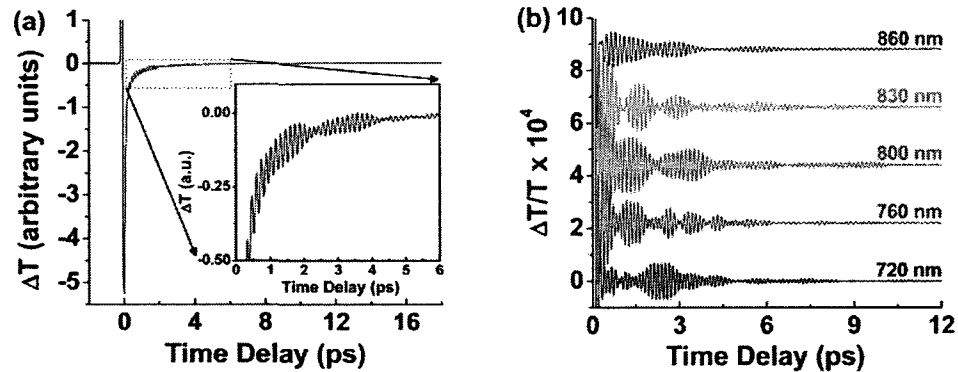


Figure 4.5 : (a) Pump-probe time-domain data taken with 800 nm center wavelength. Inset displays coherent phonon oscillations in the time-domain. (b) CP phonon oscillations measured at five different photon energies. Traces offset for clarity [44].

with RBM CPs seen with resonant Raman spectroscopy (RRS) [44].

Their sample of choice was a micelle-suspended HiPco SWNT solution. They tuned the center wavelength in 5-nm steps from 710 nm to 860 nm and excited and measured CP oscillations, as shown in Figure 4.5. The amplitude of the normalized differential transmission was  $10^{-4}$ , and each trace consisted of a superposition of many RBMs with different frequencies. This can be seen from the nature of the resulting strong beating pattern in each of the traces. The decay time for the CP oscillations was  $\sim 5$ ps.

Figure 4.6 shows both 3D and 2D plots comparing the FFT of CP oscillations obtained by CP spectroscopy and RRS. It is important to first note the overall agreement between peak positions for both techniques. However, there are distinct differences, namely the resolved peak features in CP data that can be attributed to narrower line widths compared to RRS. This allowed for more systematic identification and assignment of RBMs in the CP spectra over the 1.44eV-1.75eV photon energy range as compared with RRS.

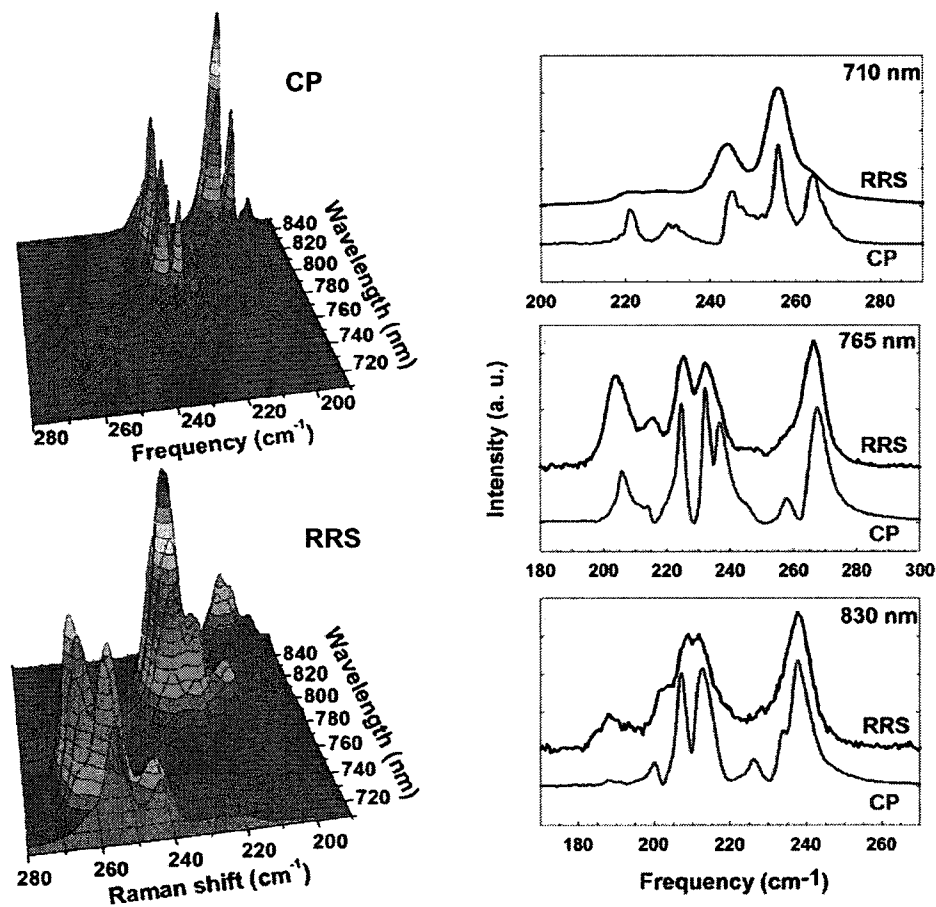


Figure 4.6 : (Left) 3D plots of FFT of CP oscillations and RRS over an excitation range of 710-850nm. (Right) 2D spectra comparing CP to RRS for three different photon energies [44].

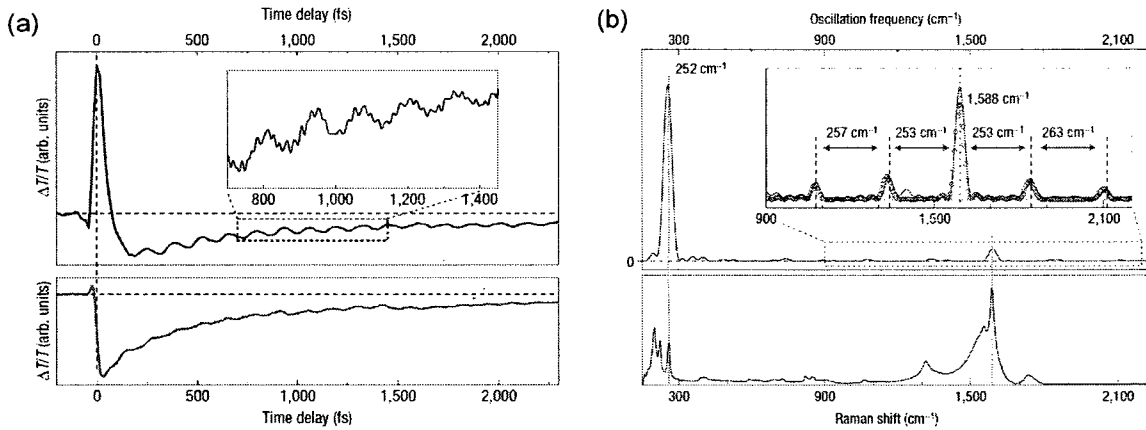


Figure 4.7 : (a) Differential transmission dynamics of SWNTs. Top panel, visible excitation energy (1.2-2.4eV), probe energy is 2.1eV. Both are sub-10-fs pulses. Bottom panel, 30-fs excitation pulse at 0.92eV and a sub-10-fs probe pulse with 2.0eV energy. (b) Vibrational spectra of SWNTs. Top panel is FFT of CP spectra from (a) and bottom panel is CW Raman spectrum for comparison [45].

Gambetta *et al.* then shortened the pulsewidth of the pump and probe to sub-10fs visible pulses to generate and detect not only the RBM CPs, but also the G mode phonons [45]. Tuning the pump wavelength, they were able to observe either initial photobleaching or photoabsorption as shown in Figure 4.7(a). This differential transmission signal includes the CP oscillations and the zoomed-in panel better illustrates the higher-order frequency oscillations that correspond to the G mode phonon. Calculating the FFT of the extracted CP oscillations, Figure 4.7(b) top panel clearly shows both RBM and G mode phonons corresponding to  $252\text{ cm}^{-1}$  and  $1588\text{ cm}^{-1}$ , respectively. The bottom panel illustrates a continuous-wave Raman spectrum for comparison with the CP spectra.

With current efforts focused on purification, separation, and enrichment of nanotubes for commercial based fabrication, Kim *et al.* utilized the technique of femtosecond pulse shaping in ultrafast pump-probe spectroscopy to selectively excite coherent

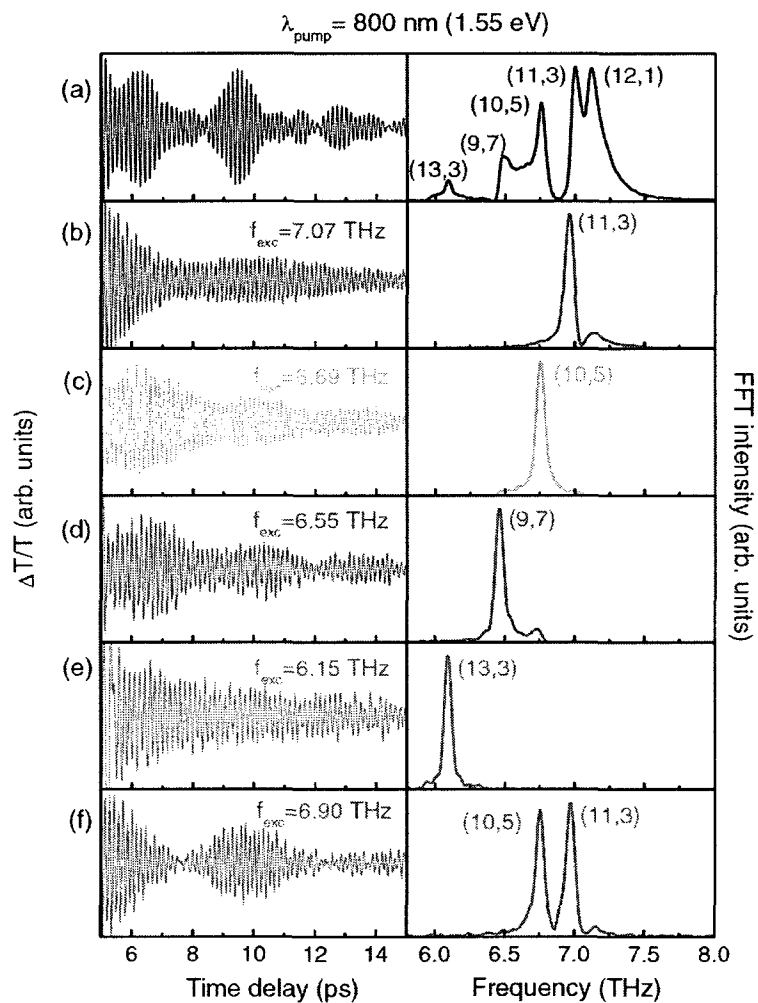


Figure 4.8 : (a) (Left) Differential transmission of ensemble solution sample without pulse-shaping. (Right) FFT of time-domain oscillations with peak assignment. (b)-(f) (Left) Differential transmission of ensemble solution with pulse-shaping. (Right) FFT of selectively excited nanotubes [49].

lattice vibrations of the RBM in SWNTs, where chirality selectivity was achieved by using multiple pulse trains, with a pulse-to-pulse interval corresponding to the period of a specific RBM [49]. As shown in Figure 4.8(a), without pulse shaping, the time domain contains the simultaneous generation of several RBM frequencies. However, applying pulse-shaping to the pump and choosing the correct repetition rate of the pulse-trains, a specific chirality can be selectively excited, as shown in Figures 4.8(b)-(f). This selectivity can then provide more accurate phase and excited state information about a specific nanotube that would otherwise be obscured with other nanotubes in the time-domain.

Expanding CP spectroscopy to investigate characteristic SWNT optical anisotropy, Kim *et al.* performed polarization dependent measurements on CP oscillations in micelle-suspended SWNT solution sample [46]. For such measurements, a half-wave plate that was rotated with a stepping motor was used on the pump, while the probe polarization was fixed with horizontal orientation. Figure 4.9 shows the polarization dependence as a function of pump angle. It should be noted that although the CP intensity decreases from  $0^\circ$  to  $90^\circ$ , the CP signal at  $90^\circ$  does not disappear, as is expected from the 1D anisotropy of the absorption. However, this is due to the nature of the sample, where a solution sample contains nanotubes oriented in random directions. As such, even if the pump polarization is perpendicular to a number of nanotubes, there are still other tubes partially aligned or completely aligned with the pump polarization at  $90^\circ$ . Therefore, to truly investigate polarization dependence, an aligned sample will be necessary. It is from here that we extend such measurements to investigate polarization anisotropy of CPs in SWNTs.

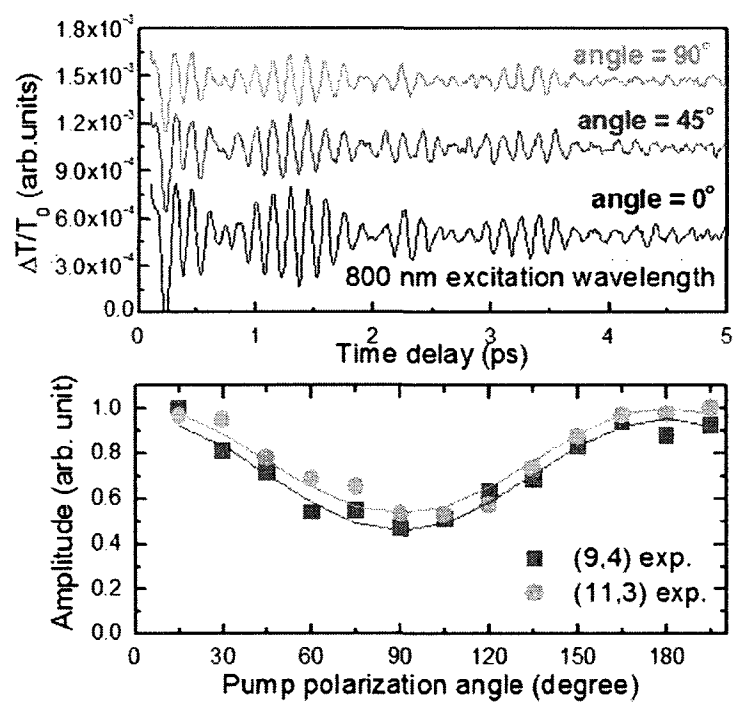


Figure 4.9 : (Top) CP oscillations for various pump polarizations. (Bottom) Amplitude of CP oscillations for the (9,4) and (11,3) nanotubes as a function of pump polarization angle [46].



### 4.3 Experimental methods

#### 4.3.1 Sample fabrication: Highly-aligned SWNTs

The sample of choice for our polarization dependent measurements are highly-aligned SWNT thin films deposited on sapphire substrates. Pint et al. has developed a unique technique to form films of highly-aligned SWNTs of various thickness directly from vertically aligned arrays of carbon nanotubes (carpets).

The film process is shown in Figure 4.10(a). First, the growth substrate undergoes optical lithography to form narrow 1-2  $\mu\text{m}$  lines of Fe/Al<sub>2</sub>O<sub>3</sub> that are separated by 50  $\mu\text{m}$ . The carpet is then grown via chemical vapor deposition (CVD) with a high temperature exposure to C<sub>2</sub>H<sub>2</sub>, H<sub>2</sub>O, and H<sub>2</sub>, and allowed to rapidly cool in the presence of acetylene [57]. After exposure, the acetylene is turned off and the carpets undergo a high temperature (775°C) H<sub>2</sub>/H<sub>2</sub>O etch to remove the SWNTs from its Fe-O catalyst base.

Once the carpet is removed from the catalyst, it can then be transferred to another surface, like sapphire in our case. This is simply done by touching the film with another surface. As the nanotubes are only weakly bound by van der Waals forces to the catalyst base, touching the film with the host substrate will layover the nanotubes, shown in step II of Figure 4.10(a). Finally, the host substrate can be lifted, removing the SWNT film from the growth substrate without any residual catalyst particles. Figures 4.10(b-c) depicts before and after images of the transfer process.

The resulting film produces aligned nanotubes of the same length, with a diameter distribution centered around 3 nm, as shown in Figure 4.11 [58]. This diameter distribution implies that our pump-probe measurements will excite higher order excitation bands around  $E_{33}$  and  $E_{44}$ . With such an aligned sample, our polarization measurements can be extended to include the sample as an additional rotation parameter.

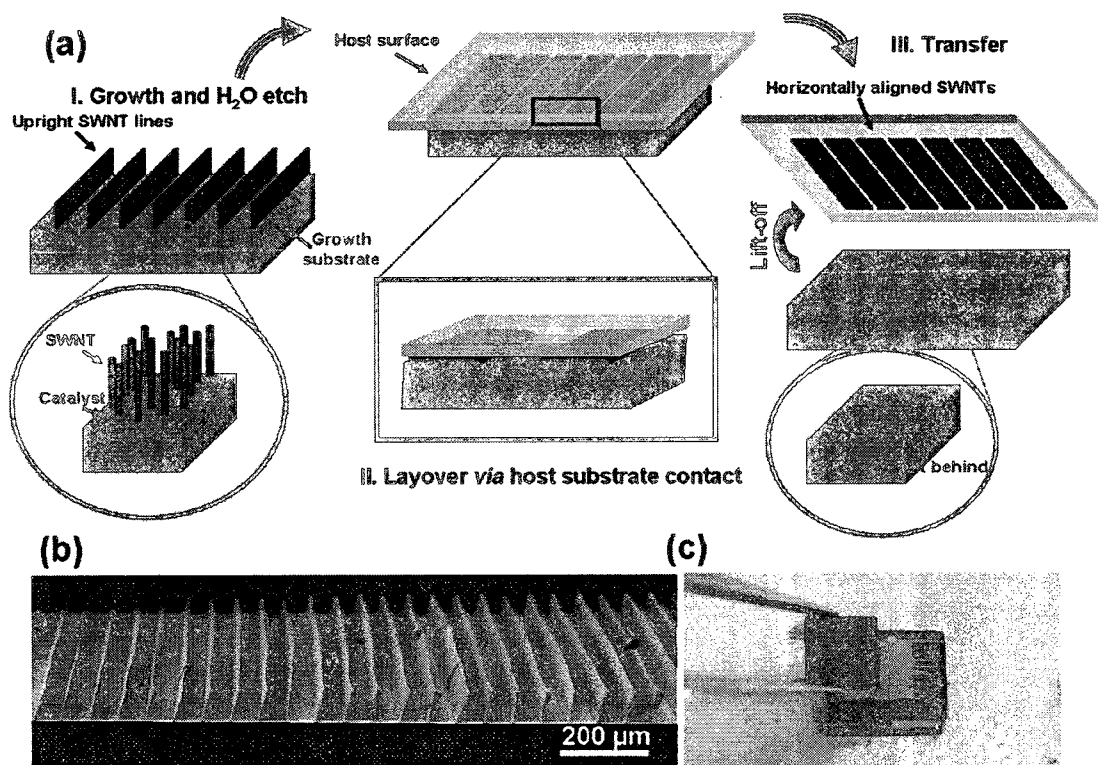


Figure 4.10 : (a) Transfer process scheme of aligned SWNT films (b) SEM image carpet arrays separated by 50  $\mu\text{m}$  prior to transfer process (c) complete transfer to diamond window[58].

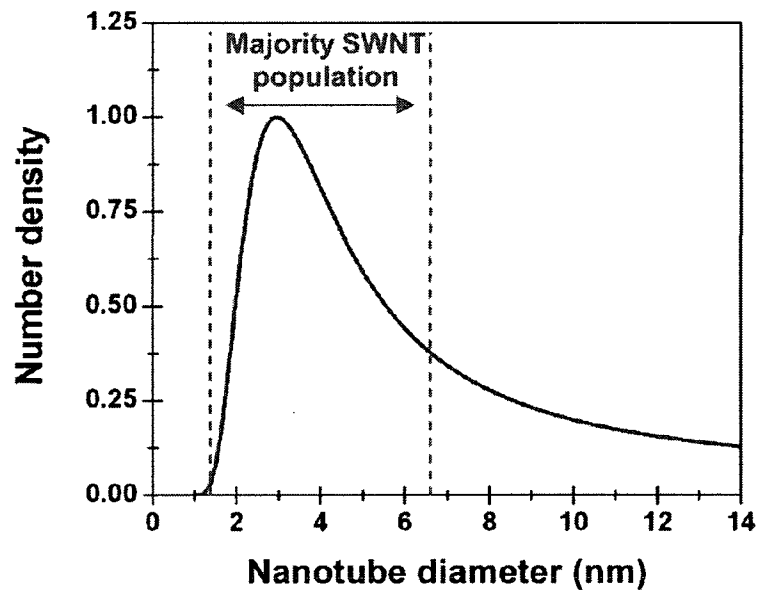


Figure 4.11 : SWNT film diameter distribution[58].

#### 4.3.2 Coherent phonon spectroscopy

Our coherent phonon spectroscopy system is a modified pump-probe spectroscopy system, where we utilize a fast scan detection scheme as opposed to the standard lock-in detection. Figure 4.12 is a schematic of our coherent phonon system. An ultrafast femtosecond laser (Kapteyn-Murnane) source is incident on a beamsplitter to produce our pump and probe beams. The Ti:Sapphire oscillator laser, pumped by a frequency doubled Nd:YVO<sub>4</sub> laser (532 nm), has a repetition rate of 76 MHz, pulse separation of 13 ns, and a pulse width of 80 fs. The repetition rate is determined by the total length of the laser cavity optical path. The pulse width is determined by the length of separation between the two prisms in the laser cavity and the amount of glass the light travels, where the prisms control Group Velocity Dispersion (GVD) compensation.

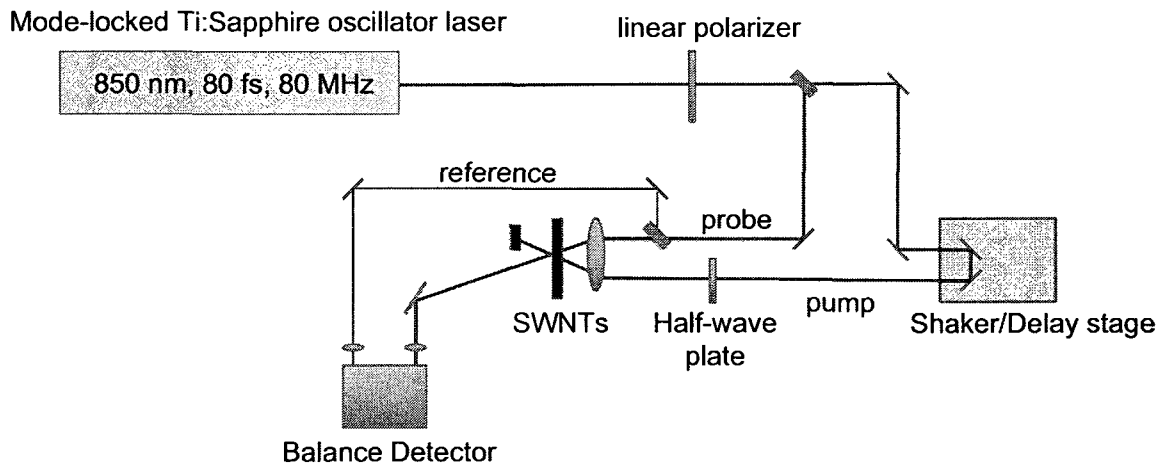


Figure 4.12 : Schematic of coherent phonon spectroscopy system.

The laser is tuned to a wavelength centered at 850 nm and because our coherent phonon system is a degenerate pump-probe system, both pump and probe beams have the same wavelength. For such a measurement where we probe nonlinear effects induced by the pump, the probe should be significantly weaker in power than the pump. We can achieve this by ensuring our beamsplitter provides at least 10:1 pump to probe power ratio.

Before it is focused on the sample, the pump beam is propagated through a shaker-delay stage that behaves as a fast scanning delay generator. In conjunction with a fast A/D (analog-to-digital) converter and optical detection, the shaker-delay stage is used to average thousands of pump-probe scans in minutes. This is extremely beneficial when signal to noise ratio is limited. For our measurements, we can resolve CP signal on the order of  $10^{-6}$ .

The motorized delay stage produces a time delay of the pump beam ( $t = \frac{2\Delta x}{c}$ ), where  $\Delta x$  is the position of shaker on the delay stage. This is fundamental in a

pump-probe system, where the shaker can be moved down the line of the delay stage to separate the pump and probe pulses in time. The position of the delay stage in which the pump and probe pulses have zero time separation, meaning they overlap exactly in time, is referred to as "timing zero". Therefore, when both the pump and probe pulses overlap in the sample at timing zero, the pump induces a maximum nonlinear effect in the sample that is detected by the probe.

As shown in Figure 4.13, the shaker controller connected to the shaker itself is driven by a function generator. For the purposes of smooth shaking motion, a sine wave is chosen with an amplitude and frequency determined by the experimental requirements (typically 6Vpp, 15Hz for our CP measurements). The shaker controller output is then sent to an A/D converter to provide temporal information about the shaker position. The pump-probe signal from the Nirvana balance detector output is also connected to the A/D converter, but only after connection to a current pre-amplifier. The A/D converter is finally connected to a computer and Labview software is used to average and record data. The recorded time axis is determined by the shaking amplitude of the shaker.

Separate from the pump beam, the probe is focused and spatially overlapped with the pump on the sample after it is transmitted through a second beamsplitter. Here, the reflected beam from the beamsplitter is called the reference beam and does not interact with the sample. Instead, the reference beam is illuminated on one of the two Si photodiodes of the Nirvana balance detector. The other Si photodiode is illuminated by the transmitted probe after the sample.

The Nirvana balance detector monitors the optical power of the probe and reference and has four distinct settings: *LINEAR*, *BAL*, *AutoBAL*, and *10X*. The *LINEAR* output is solely the voltage proportional to the optical power of the probe, while *BAL* is the voltage proportional to the difference between the probe and reference. *Auto-*

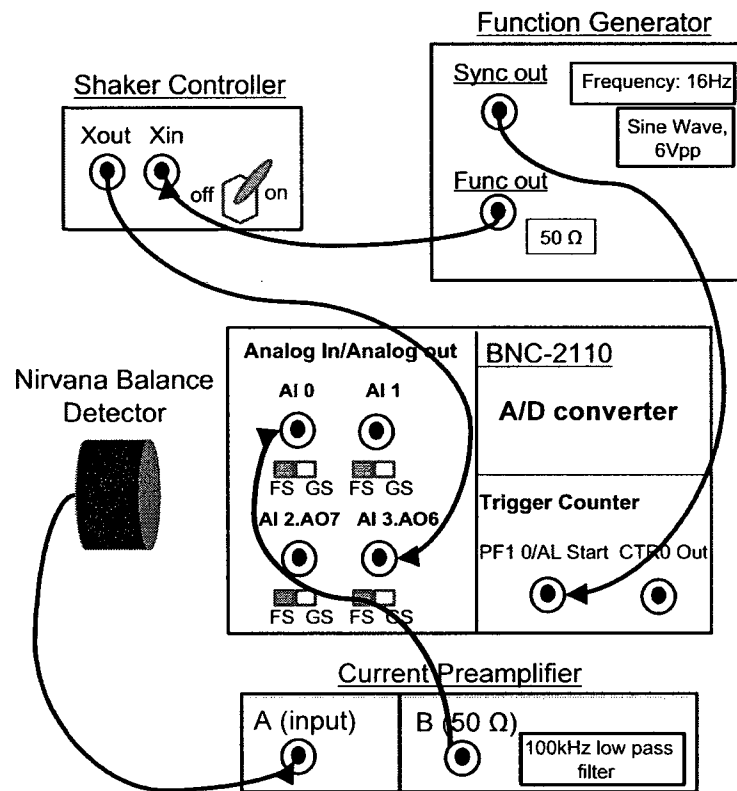


Figure 4.13 : Schematic of A/D converter connections and fast scan detection.

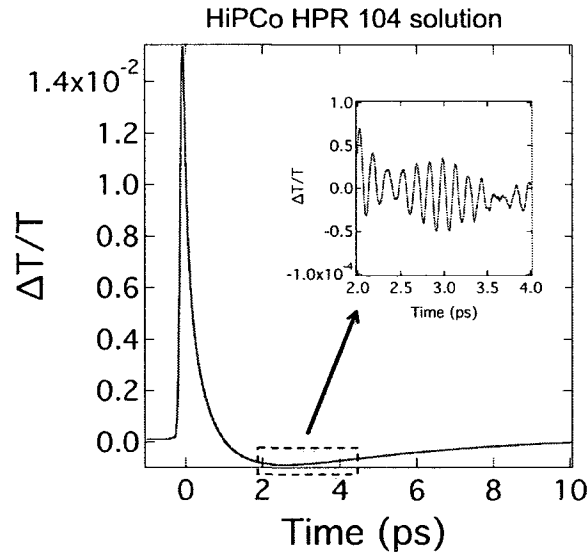


Figure 4.14 : Differential transmission of the time-domain pump-probe signal. Inset includes CP oscillations in the time-domain.

*BAL* is autobalanced detection, where the output is proportional to the optical power of the probe after common noise between the probe and reference is removed. This is highly beneficial when signal is small compared to the noise in the experiment. *10X* is the autobalanced setting with a gain of 10. For our measurements, *10X* is used.

Typical pump-probe time-domain signal with CP oscillations from a HiPCo solution sample is shown in Figure 4.14. The zoomed in panel emphasizes our ability to monitor real-time CP oscillations with our detection scheme.

The underlying physics that provides the mechanism to detect CP oscillations can be qualitatively explained. When the pump is incident on a SWNT sample with adequate energy to excite carriers across the band gap into higher order energy levels in the conduction band, these excited carriers will eventually perform intraband relaxation, relaxing to the bottom of the conduction band. This is a nonradiative decay channel mediated by phonons, and due to the pulse width of our pump pulses

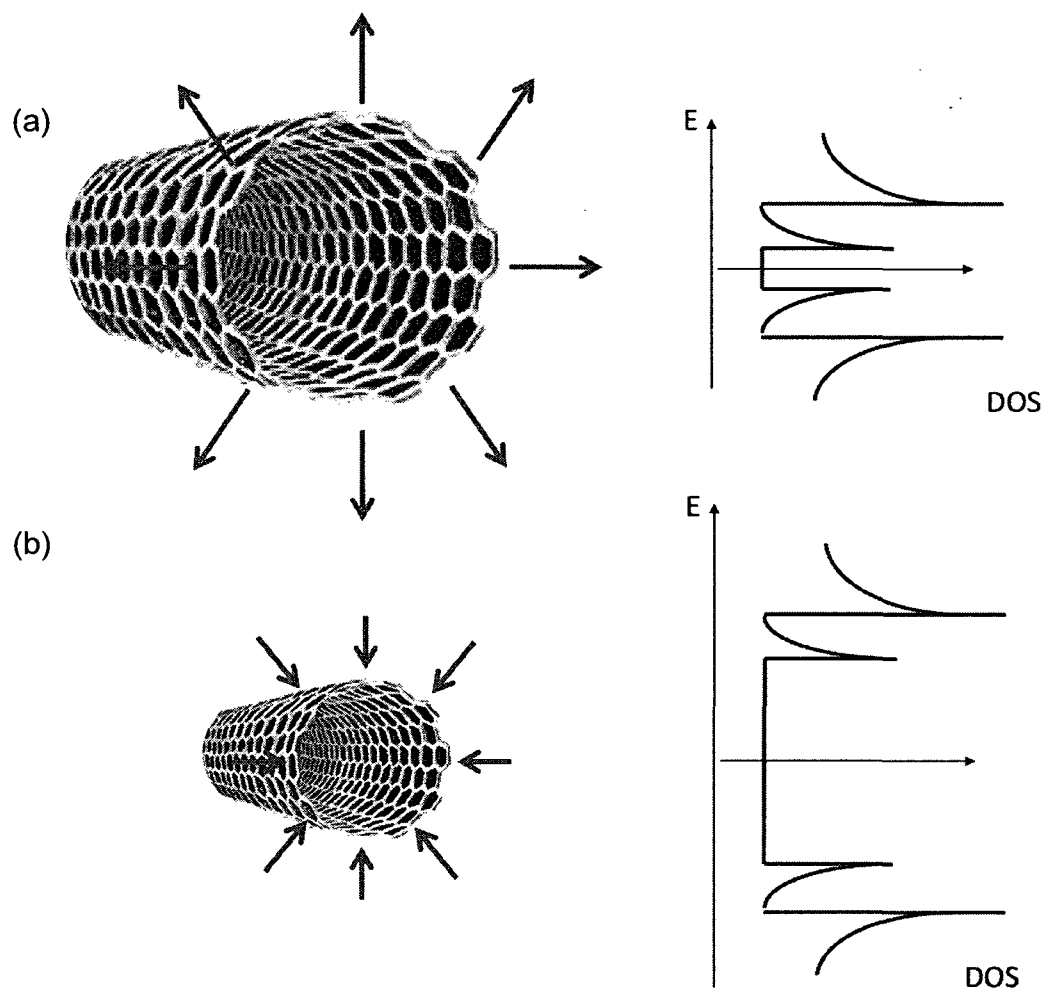


Figure 4.15 : Oscillation of nanotube diameter and nanotube band gap. (a) As the nanotube diameter expands, the band gap shrinks. (b) As the nanotube diameter shrinks, the band gap expands.



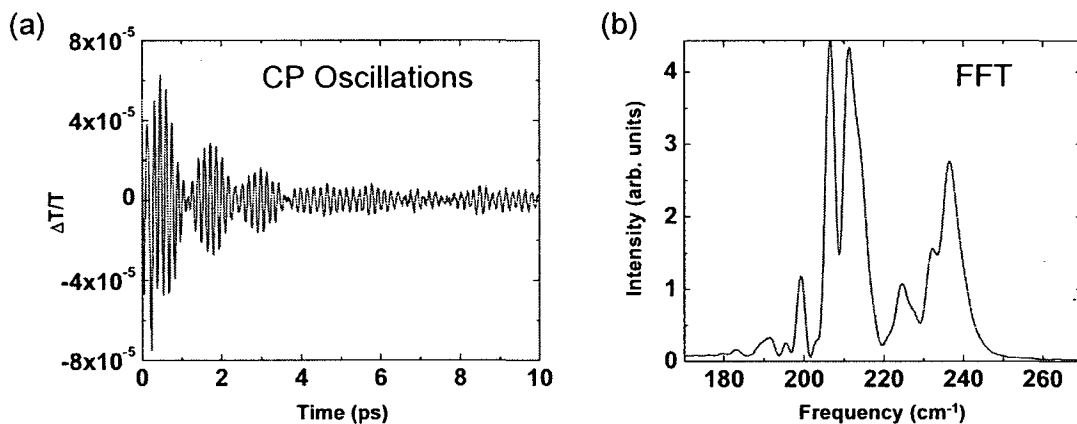


Figure 4.16 : (a) Time-domain signal of extracted CP oscillations. (b) FFT of time-domain of CP oscillations.

exciting the sample, the specific phonons involved are RBM phonons. Once carriers transfer energy to the RBM phonons, the RBM phonon oscillations are induced in the SWNT sample.

Considering the case of a single nanotube, as the RBM oscillates, the nanotube diameter oscillates, and the band gap of the nanotube will also oscillate with  $E_{ii} \sim \frac{1}{d}$ , where  $d$  is nanotube diameter [59]. In Figure 4.15(a), when the nanotube diameter expands, the band gap shrinks. The opposite is seen in Figure 4.15(b), where the band gap opens when the nanotube diameter shrinks.

This phenomenon can then be observed optically because as the size of the band gap oscillates, more or less pump light can be absorbed and monitored by the probe. The transmitted pump-probe signal will then oscillate exactly with the induced RBM phonon. For the case of an ensemble of nanotubes close in diameter, the oscillations will manifest itself as beating in the time-domain, as shown in Figure 4.16(a).

To extract the CP oscillations from the characteristic pump-probe background, the pump probe signal is first fit with a number of exponentials.

This exponential fit is then subtracted from the pump probe signal and the resulting CP oscillations (as shown in Figure 4.16(a)) remains. Performing a Fast-Fourier transformation from the time-domain to the frequency domain allows us to determine the exact frequencies of nanotubes in the ensemble (Figure 4.16(b)).

### 4.3.3 Polarization dependence

Figure 4.17 (a) shows the UV-VIS absorption spectrum of a typical aligned sample, while Figure 4.17 (b) shows the THz absorbance spectrum. The polarization anisotropy is obvious in the THz regime, as there is virtually zero absorption when the sample is perpendicular to the THz polarization. Therefore, with such an aligned sample, our polarization measurements can be extended to include the sample as an additional rotation parameter.

As depicted in Figure 4.18, two types of polarization measurements were investigated. Type I measurements maintained the same polarization for the pump and probe, while rotating the alignment axis of the sample. Type II measurements maintained the same orientation for the probe and sample, while rotating the pump polarization. For Type II measurements, a half-wave plate provided 90-degree rotation of the pump.

## 4.4 Experimental results

Performing polarization dependent coherent phonon spectroscopy, we begin by first rotating the sample in Type I configuration and monitoring the pump-probe signal. Figure 4.19 shows the resulting polarization dependence of the pump probe at  $0^\circ$ ,  $45^\circ$ , and  $90^\circ$ . It is clear that there is a distinct polarization dependence, as we see a decrease in differential transmission of the electronic component as the sample is rotated by 90 degrees.

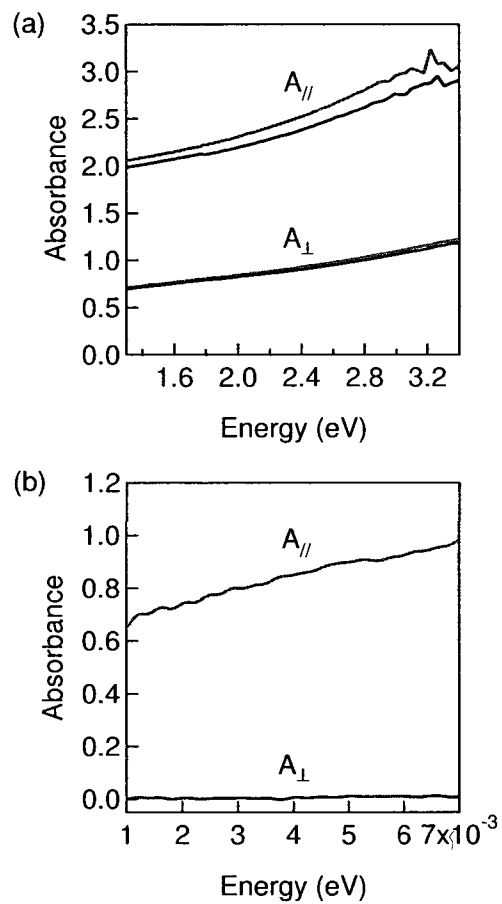


Figure 4.17 : (a) UV-VIS Absorption spectrum of CVD grown aligned SWNTs at  $0^\circ$  and  $90^\circ$  to light polarization. (b) THz absorbance spectrum for the aligned SWNT film at  $0^\circ$  and  $90^\circ$  to THz polarization.

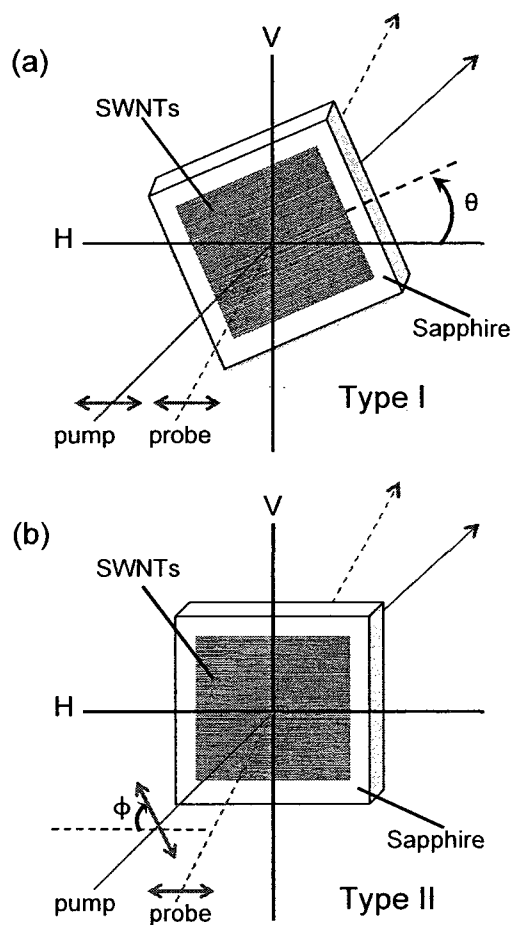


Figure 4.18 : SEM image of aligned SWNTs and experimental configurations are shown. (a) For Type I, pump and probe polarizations are fixed and sample orientation is rotated. (b) For Type II, probe and sample orientations are fixed and pump polarization is rotated.

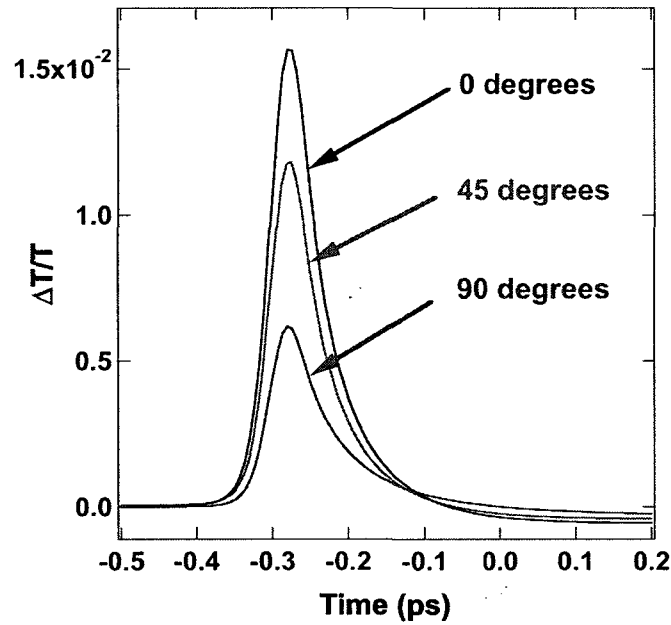


Figure 4.19 : Polarization dependence of pump-probe signal in Type I orientation.

Our polarization dependent results for both Type I and Type II orientations are shown in Figures 4.20 and 4.21. Here, the differential transmission amplitude of the RBM CP oscillations is on the order of  $10^{-6}$ , with a CP decay time of  $\sim 1.5$ ps. This short decay time is expected with our sample of highly-bundled SWNTs. As the polarization angle is rotated, we see a strong polarization anisotropy of the RBM CPs as a function of angle, where the strongest oscillations at  $0^\circ$  are completely quenched at  $90^\circ$  for both types.

## 4.5 Analysis and discussion

To produce the CP spectra (Figure 4.22), we calculate the fast Fourier transformation (FFT) of the CP oscillations in the time-domain. The frequencies of the CP oscilla-

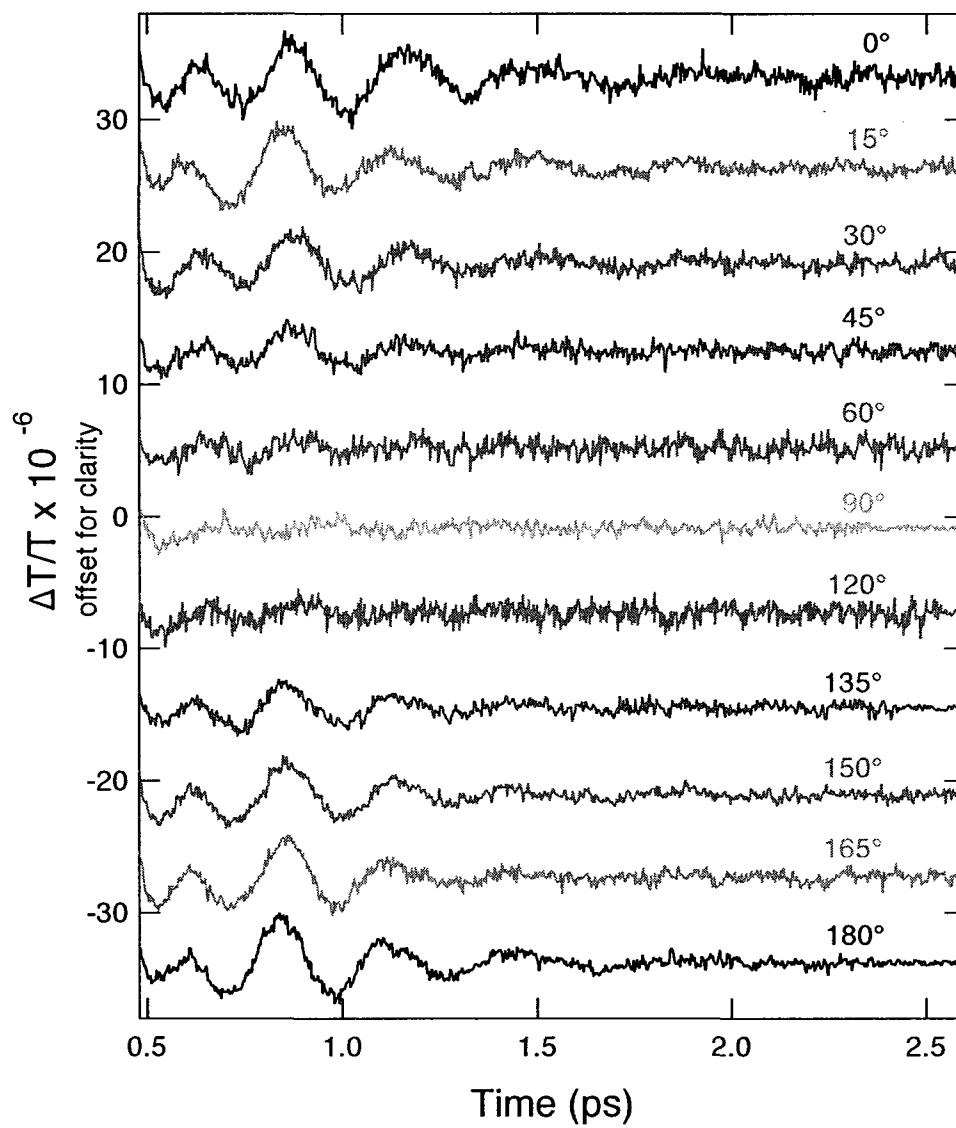


Figure 4.20 : Polarization dependence of CP signal in Type I orientation.

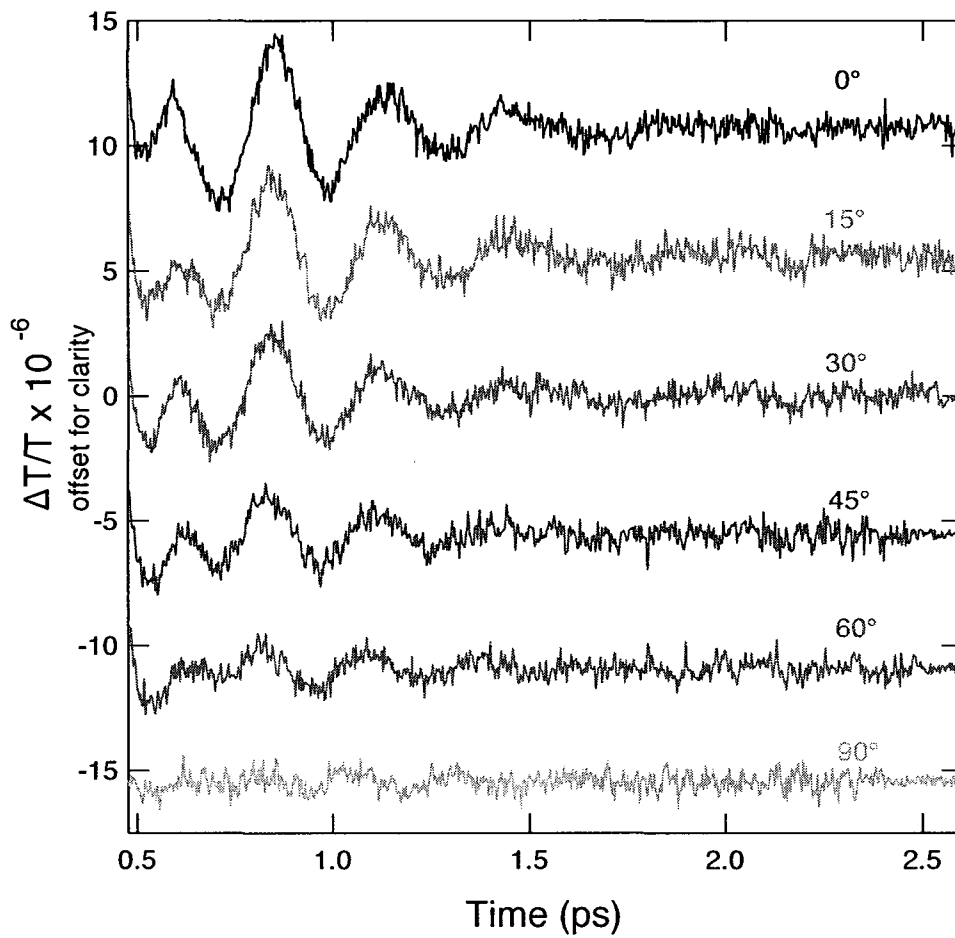


Figure 4.21 : Polarization dependence of CP signal in Type II orientation.

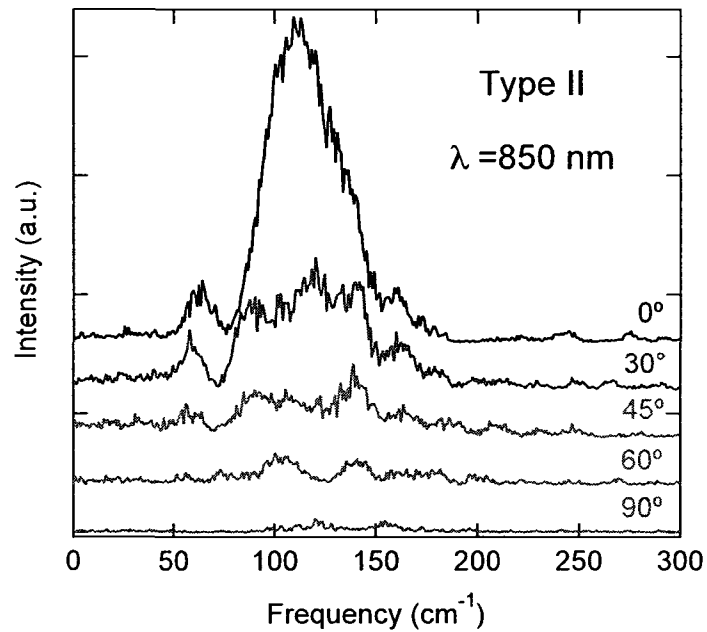


Figure 4.22 : Polarized CP spectrum for Type II. The traces are offset for clarity.

tions range from 50-200  $\text{cm}^{-1}$ , and is consistent with the large diameter distribution of nanotubes within the sample. The polarization anisotropy is obvious both in the CP spectra and also for the various nanotubes that are excited.

Figure 4.23 plots the integrated CP intensity of the FFT for all excited nanotubes and includes fits of  $\cos^4\theta$ , where  $\theta$  is the angle of rotation for the Type I sample polarization and for the Type II pump polarization. Such a fit is typical for polarization dependence measurements of Raman in perfectly aligned nanotubes [7]. Both Type I and Type II results fit well with  $\cos^4\theta$ , indicating a highly-aligned sample even though our sample is largely bundled, and we can now extend these results to determine the nematic order parameter,  $S$ , to quantitatively calculate the degree of alignment of our nanotubes. The analysis and corresponding theory were calculated by Dr. Gary Sanders and Dr. Christopher Stanton at the University of Florida [60].



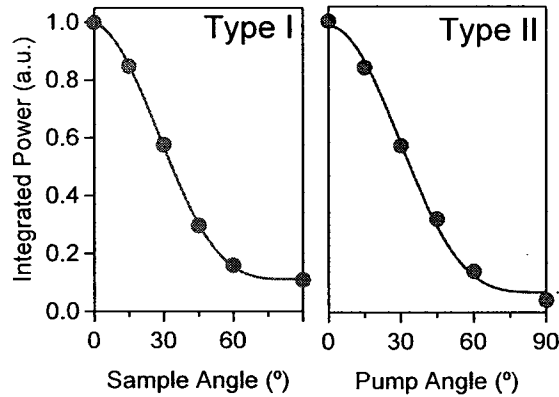


Figure 4.23 : Integrated CP intensity as a function of angle for Type I and Type II. The solid lines are fits to  $\cos^4\theta$ , expected when nanotubes are perfectly aligned.

To calculate the nematic order parameter, we first assume that the nanotube alignment angles on the sapphire substrate are described by a Gaussian distribution function with a small standard deviation  $\Delta\theta$ . Then, the angle between the pump polarization and the averaged nanotube axis is  $\theta$  and  $\vartheta$  between the pump and each nanotube axes is described by

$$P(\vartheta, \theta, \Delta\theta) = \frac{1}{\sqrt{2\pi}(\Delta\theta)} \exp\left(-\frac{(\vartheta - \theta)^2}{2(\Delta\theta)^2}\right) \quad (4.3)$$

Subsequently, as the integrated CP power for each nanotube is  $A \cos^p(\vartheta)$ , then the entire ensemble integrated power  $I_{cp}(\theta, \Delta\theta)$  is

$$I_{cp}(\theta, \Delta\theta) = A \int_{-\infty}^{\infty} d\vartheta P(\vartheta, \theta, \Delta\theta) \cos^p(\vartheta) \quad (4.4)$$

For Type II results,  $\theta$  is replaced by  $\phi$  for both equations above. Solving this analytically, the results are shown in Figure 4.24, where  $p = 8$  for Type I and  $p = 4$

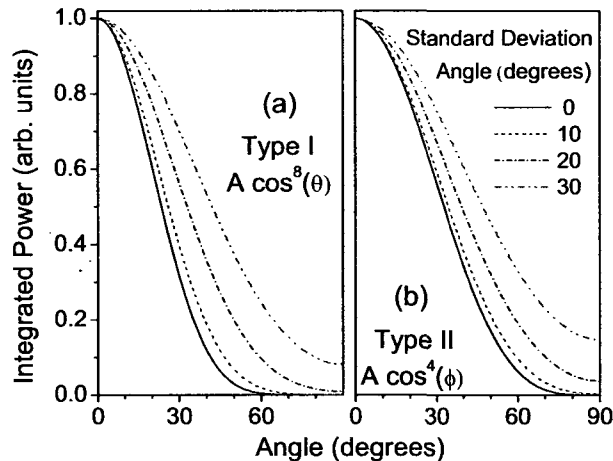


Figure 4.24 : Misalignment effects on the integrated CP power [60].

for Type II. We can see that as  $\Delta\theta$  [ $\Delta\phi$ ] increase, quenching of the CP intensity is reduced.

We can now fit our experimental results by assuming a fitting function of  $A \cos^p(\theta + \Delta\theta) + B [A \cos^p(\phi + \Delta\phi) + B]$ , where  $A$  and  $B$  are background subtraction and rescaling parameters,  $\Delta\theta$  [ $\Delta\phi$ ] is a random Gaussian distributed misalignment angle (standard deviation  $\Delta\theta$  [ $\Delta\phi$ ]), and  $p = 8$  for Type I and  $p = 4$  for Type II. Calculating these fits with the same standard deviation for nanotube misalignment angles for both Type I and Type II, our results are shown in Figure 4.25, where the standard deviation is  $\Delta\theta = \Delta\phi = 18.7^\circ$ .

We can now calculate the nematic order parameter,  $S$ , a dimensionless quantity that measures the degree of alignment, where  $S = 0$  is for a randomly oriented sample and  $S = 1$  is for a completely aligned sample. Calculating the nematic order parameter,  $S$ , for small  $\Delta\theta$  is  $S = \exp(-2 (\Delta\theta)^2) = 0.81$ .

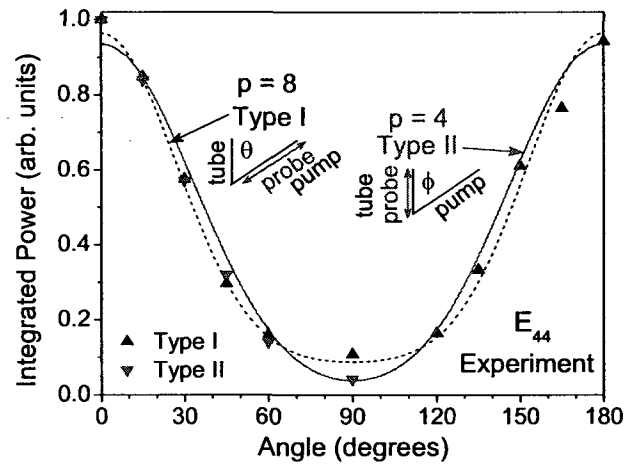


Figure 4.25 : Experimental results fit to  $A \cos^p(\theta + \Delta\theta) + B$  for Type I and  $A \cos^p(\phi + \Delta\phi) + B$  for Type II [60].

## Chapter 5

### Conclusion

To further understand the role of excitons and phonons in SWNTs, we have successfully performed both mK magneto-PL and CP spectroscopy. Our mK results showed that at low temperatures, current theory does not adequately explain the zero-field PL and magnetic brightening. We also showed that including disorder into the current theory also does not account for the mK magnetic brightening. Only when we considered a non-thermal distribution of excitons, did our experimental results fit successfully to our new theory, and we discovered a large population of excitons still in the bright state. This opens the door for more experiments, especially temperature dependent measurements to improve our new theory and determine the exact form of the  $R$ , the non-thermal excitonic population coefficient.

Finally, for our CP measurements in Chapter 4, we investigated the polarization anisotropy of coherent phonon dynamics in highly-aligned single-walled carbon nanotubes and measured RBM coherent phonons as a function of polarization angle. We saw a complete quenching of the RBM for both geometries and extended our results to determine the degree of alignment of the sample. Including misalignment effects to our fitting, we determined the nematic order parameter to be 0.81. Our results are the first polarization anisotropy study of CPs in highly-aligned SWNT thin films.

## Bibliography

- [1] A. Jorio, G. Dresselhaus, and M. S. Dresselhaus, *Carbon Nanotubes: Advanced Topics in the Synthesis, Structure, Properties and Applications* (Springer, Berlin, 2008).
- [2] G. S. Duesberg, I. Loa, M. Burghard, K. Syassen, and S. Roth, "Polarized Raman spectroscopy on isolated single-wall carbon nanotubes," *Phys. Rev. Lett.* **85**, 5436 (Jan 2000).
- [3] A. Jorio, G. Dresselhaus, M. S. Dresselhaus, M. Souza, M. S. S. Dantas, M. A. Pimenta, A. M. Rao, R. Saito, C. Liu, and H. M. Cheng, "Polarized Raman study of single-wall semiconducting carbon nanotubes," *Phys. Rev. Lett.* **85**, 2617 (Jan 2000).
- [4] A. Hartschuh, H. N. Pedrosa, L. Novotny, and T. D. Krauss, "Simultaneous fluorescence and Raman scattering from single carbon nanotubes," *Science* **301**, 1354 (Jan 2003).
- [5] Z. M. Li, Z. K. Tang, H. J. Liu, N. Wang, C. T. Chan, R. Saito, S. Okada, G. F. Li, J. S. Chen, N. Nagasawa, and S. Tsuda, "Polarized Absorption Spectra of Single-Walled 4 Å Carbon Nanotubes Aligned in Channels of an AlPO<sub>4-5</sub> Single Crystal," *Phys. Rev. Lett.* **87**, 127401 (Aug 2001).
- [6] M. F. Islam, D. E. Milkie, C. L. Kane, A. G. Yodh, and J. M. Kikkawa, "Direct measurement of the polarized optical absorption cross section of single-wall

- carbon nanotubes,” *Phys. Rev. Lett.* **93**, 037404 (Jan 2004).
- [7] H. H. Gommans, J. W. Alldredge, H. Tashiro, J. Park, J. Magnuson, and A. G. Rinzler, “Fibers of aligned single-walled carbon nanotubes: Polarized Raman spectroscopy,” *J. Appl. Phys.* **88**, 2509 (Jan 2000).
- [8] T. A. Searles, Y. Imanaka, T. Takamasu, H. Ajiki, J. A. Fagan, E. K. Hobbie, and J. Kono, “Large Magnetic Susceptibility Anisotropy of Metallic Carbon Nanotubes,” arXiv **1001.0524v1** (Jan 2010), 4 pages, 4 figures.
- [9] H. Ajiki and T. Ando, “Magnetic Properties of Carbon Nanotubes,” *J. Phys. Soc. Jpn.* **62**, 2470 (1993).
- [10] M. A. L. Marques, M. d’Avezac, and F. Mauri, “Magnetic response and NMR spectra of carbon nanotubes from ab initio calculations,” *Phys. Rev. B* **73**, 125433 (Mar 2006).
- [11] J. P. Lu, “Novel Magnetic Properties of Carbon Nanotubes,” *Phys. Rev. Lett.* **74**, 1123 (Feb 1995).
- [12] M. F. Islam, D. E. Milkie, O. N. Torrens, A. G. Yodh, and J. M. Kikkawa, “Magnetic heterogeneity and alignment of single wall carbon nanotubes,” *Phys. Rev. B* **71**, 201401 (Jan 2005).
- [13] S. Zaric, G. N. Ostojic, J. Kono, J. Shaver, V. C. Moore, R. H. Hauge, R. E. Smalley, and X. Wei, “Estimation of Magnetic Susceptibility Anisotropy of Carbon Nanotubes Using Magnetophotoluminescence,” *Nano Lett.* **4**, 2219 (Jan 2004).
- [14] S. Zaric, G. N. Ostojic, J. Kono, J. Shaver, V. C. Moore, M. S. Strano, R. H. Hauge, R. E. Smalley, and X. Wei, “Optical signatures of the Aharonov-Bohm phase in single-walled carbon nanotubes,” *Science* **304**, 1129 (May 2004).

- [15] J. Shaver, A. N. G. Parra-Vasquez, S. Hansel, O. Portugall, C. H. Mielke, M. von Ortenberg, R. H. Hauge, M. Pasquali, and J. Kono, "Alignment Dynamics of Single-Walled Carbon Nanotubes in Pulsed Ultrahigh Magnetic Fields," *ACS Nano* **3**, 131 (Jan 2009).
- [16] L. Ren, C. L. Pint, L. G. Booshehri, W. D. Rice, X. Wang, D. J. Hilton, K. Takeya, I. Kawayama, M. Tonouchi, R. H. Hauge, and J. Kono, "Carbon Nanotube Terahertz Polarizer," *Nano Lett.* **9**, 2610 (Jan 2009).
- [17] M. S. Dresselhaus, G. Dresselhaus, and P. C. Eklund, *Science of Fullerenes and Carbon Nanotubes* (Academic Press, New York, 1996).
- [18] M. S. Dresselhaus, G. Dresselhaus, and R. Saito, "Carbon fibers based on C60 and their symmetry," *Phys. Rev. B* **45**, 6234 (Jan 1992).
- [19] M. S. Dresselhaus and P. C. Eklund, "Phonons in carbon nanotubes," *Advances in Physics* **49**, 705 (Dec 2000).
- [20] R. Saito, G. Dresselhaus, and M. S. Dresselhaus, *Physical properties of carbon nanotubes* (World Scientific, Singapore, 2003).
- [21] R. Saito, M. Fujita, G. Dresselhaus, and M. S. Dresselhaus, "Electronic structure of chiral graphene tubules," *Appl. Phys. Lett.* **60**, 2204 (Jan 1992).
- [22] R. Saito, M. Fujita, G. Dresselhaus, and M. S. Dresselhaus, "Electronic structure of graphene tubules based on C60," *Phys. Rev. B* **46**, 1804 (Jan 1992).
- [23] T. Ogawa, *Optical properties of low-dimensional materials*, Ed. by T. Ogawa, Y. Kanemitsu (World Scientific Publishing Co. Pte Ltd, Singapore, 1995).
- [24] R. Loudon, "One-dimensional hydrogen atom," *Am. J. Phys.* **27**, 649 (1959).

- [25] F. Wang, G. Dukovic, L. E. Brus, and T. F. Heinz, "The optical resonances in carbon nanotubes arise from excitons," *Science* **308**, 838 (Jan 2005).
- [26] J. Maultzsch, R. Pomraenke, S. Reich, E. Chang, D. Prezzi, A. Ruini, E. Molinari, M. S. Strano, C. Thomsen, and C. Lienau, "Exciton binding energies in carbon nanotubes from two-photon photoluminescence," *Phys. Rev. B* **72**, 241402 (Jan 2005).
- [27] J. Shaver and J. Kono, "Temperature-dependent magneto-photoluminescence spectroscopy of carbon nanotubes: evidence for dark excitons," *Laser & Photon. Rev.* **1**, 260 (Dec 2007).
- [28] C. D. Spataru, S. Ismail-Beigi, R. B. Capaz, and S. G. Louie, "Theory and ab initio calculation of radiative lifetime of excitons in semiconducting carbon nanotubes," *Phys. Rev. Lett.* **95**, 247402 (Jan 2005).
- [29] H. Akiyama, S. Koshihara, T. Someya, K. Wada, H. Noge, Y. Nakamura, T. Inoshita, A. Shimizu, and H. Sakaki, "Thermalization Effect on Radiative Decay of Excitons in Quantum Wires," *Phys. Rev. Lett.* **72**, 924 (Jan 1994).
- [30] D. S. Citrin, "Long Intrinsic Radiative Lifetimes of Excitons in Quantum Wires," *Phys. Rev. Lett.* **69**, 3393 (Jan 1992).
- [31] V. Perebeinos, J. Tersoff, and P. Avouris, "Radiative lifetime of excitons in carbon nanotubes," *Nano Lett.* **5**, 2495 (Jan 2005).
- [32] H. Ajiki and T. Ando, "Aharonov-Bohm Effect in Carbon Nanotubes," *Physica B* **201**, 349 (Jan 1994).
- [33] S. Roche, G. Dresselhaus, M. S. Dresselhaus, and R. Saito, "Aharonov-Bohm spectral features and coherence lengths in carbon nanotubes," *Phys. Rev. B* **62**,



- 16092 (Jan 2000).
- [34] H. Ajiki and T. Ando, "Electronic States of Carbon Nanotubes," *J. Phys. Soc. Jpn.* **62**, 1255 (Jan 1993).
- [35] S. Zaric, G. N. Ostojic, J. Shaver, J. Kono, O. Portugall, P. H. Frings, G. L. J. A. Rikken, M. Furis, S. A. Crooker, X. Wei, V. C. Moore, R. H. Hauge, and R. E. Smalley, "Excitons in carbon nanotubes with broken time-reversal symmetry," *Phys. Rev. Lett.* **96**, 016406 (Jan 2006).
- [36] J. Shaver, J. Kono, O. Portugall, V. Krstic, G. L. J. A. Rikken, Y. Miyauchi, S. Maruyama, and V. Perebeinos, "Magnetic brightening of carbon nanotube photoluminescence through symmetry breaking," *Nano Lett.* **7**, 1851 (Jan 2007).
- [37] R. A. Jishi, L. Venkataraman, M. S. Dresselhaus, and G. Dresselhaus, "Phonon modes in Carbon Nanotubules," *Chem. Phys. Lett.* **209**, 77 (Jan 1993).
- [38] A. Srivastava, H. Htoon, V. I. Klimov, and J. Kono, "Direct observation of dark excitons in individual carbon nanotubes: Inhomogeneity in the exchange splitting," *Phys. Rev. Lett.* **101**, 087402 (Jan 2008).
- [39] T. Murphy, "Dilution Refrigerators," National High Magnetic Field Laboratory, Online Animation, Accessed on 23 May 2010, <http://www.magnet.fsu.edu/education/tutorials/tools/dilutionfridge.html> (2010).
- [40] "KelvinMX : Dilution refrigerator with modular design," Oxford Instruments, Online Figure, Accessed on 24 May 2010 <http://www.oxford-instruments.com/products/low-temperature/dilution-refrigerators/kelvinmx/Pages/kelvinmx.aspx> (2010).

- [41] M. Fox, *Optical Properties of Solids* (Oxford University Press, New York, 2001).
- [42] I. B. Mortimer and R. J. Nicholas, "Role of Bright and Dark Excitons in the Temperature-Dependent Photoluminescence of Carbon Nanotubes," *Phys. Rev. Lett.* **98**, 027404 (Dec 2007).
- [43] J. Shaver, S. A. Crooker, J. A. Fagan, E. K. Hobbie, N. Ubrig, O. Portugall, V. Perebeinos, P. Avouris, and J. Kono, "Magneto-optical spectroscopy of highly aligned carbon nanotubes: Identifying the role of threading magnetic flux," *Phys. Rev. B* **78**, 081402 (Aug 2008).
- [44] Y.-S. Lim, K.-J. Yee, J.-H. Kim, E. H. Házoz, J. Shaver, J. Kono, S. K. Doorn, R. H. Hauge, and R. E. Smalley, "Coherent lattice vibrations in single-walled carbon nanotubes," *Nano Lett.* **6**, 2696 (Dec 2006).
- [45] A. Gambetta, C. Manzoni, E. Menna, M. Meneghetti, G. Cerullo, G. Lanzani, S. Tretiak, A. Piryatinski, A. Saxena, R. L. Martin, and A. R. Bishop, "Real-time observation of nonlinear coherent phonon dynamics in single-walled carbon nanotubes," *Nature Physics* **2**, 515 (Dec 2006).
- [46] J.-H. Kim, J. Park, B. Y. Lee, D. Lee, K.-J. Yee, Y.-S. Lim, L. G. Booshehri, E. H. Házoz, J. Kono, and S.-H. Baik, "Polarization anisotropy of transient carrier and phonon dynamics in carbon nanotubes," *J. Appl. Phys.* **105**, 103506 (Dec 2009).
- [47] G. D. Sanders, C. J. Stanton, J.-H. Kim, K.-J. Yee, Y.-S. Lim, E. H. Házoz, L. G. Booshehri, J. Kono, and R. Saito, "Resonant coherent phonon spectroscopy of single-walled carbon nanotubes," *Phys. Rev. B* **79**, 205434 (Dec 2009).
- [48] K. Kato, K. Ishioka, M. Kitajima, J. Tang, R. Saito, and H. Petek, "Coherent

- Phonon Anisotropy in Aligned Single-Walled Carbon Nanotubes.” *Nano Lett.* **8**, 3102 (Dec 2008).
- [49] J.-H. Kim, K.-J. Han, N.-J. Kim, K.-J. Yee, Y.-S. Lim, G. D. Sanders, C. J. Stanton, L. G. Booshehri, E. H. Háróz, and J. Kono, “Chirality-Selective Excitation of Coherent Phonons in Carbon Nanotubes by Femtosecond Optical Pulses,” *Phys. Rev. Lett.* **102**, 037402 (Jan 2009).
- [50] K. Ishioka and O. V. Misochko, *Coherent Lattice Oscillations in Solids and Their Optical Control. Part I. Fundamentals and Optical Detection Techniques*, ed. by K. Yamanouchi, A. Giulietti, K. Ledingham. Progress in Ultrafast Intense Laser Science V (Springer, Berlin, 2010).
- [51] T. Derkorsy, G. C. Cho, and H. Kurz, *Coherent Phonons in Condensed Media*, ed. by M. Cardona, G. Guntherodt. Light Scattering in Solids VIII (Springer, Berlin, 2000).
- [52] M. Först and T. Dekorsy, *Coherent Phonons in Bulk and Low-Dimensional Semiconductors*, ed. by S. De Silvestri, G. Cerullo, G. Lanzani. Coherent Vibrational Dynamics (CRC, Boca Raton, 2007).
- [53] Y. Matsumoto and K. Watanabe, “Coherent vibrations of adsorbates induced by femtosecond laser excitation,” *Chem. Rev.* **106**, 4234 (Jan 2006).
- [54] K. Ishioka, M. Kitajima, and O. V. Misochko, “Coherent A(1g) and E-g Phonons of Antimony,” *J. Appl. Phys.* **103**, 123505 (Jan 2008).
- [55] K. Ishioka, M. Kitajima, and O. V. Misochko, “Temperature Dependence of Coherent A(1g) and E-g Phonons of Bismuth,” *J. Appl. Phys.* **100**, 093501 (Jan 2006).

- [56] K. Ishioka, M. Hase, M. Kitajima, and H. Petek, "Coherent optical phonons in diamond," *Appl. Phys. Lett.* **89**, 231916 (Jan 2006).
- [57] C. L. Pint, Y.-Q. Xu, M. Pasquali, and R. H. Hauge, "Formation of highly dense aligned ribbons and transparent films of single-walled carbon nanotubes directly from carpets," *ACS Nano* **2**, 1871 (Jan 2008).
- [58] C. L. Pint, Y.-Q. Xu, S. Moghazy, T. Cherukuri, N. T. Alvarez, E. H. Házoz, S. Mahzooni, S. K. Doorn, J. Kono, M. Pasquali, and R. H. Hauge, "Dry Contact Transfer Printing of Aligned Carbon Nanotube Patterns and Characterization of Their Optical Properties for Diameter Distribution and Alignment," *ACS Nano* **4**, 1131 (2010).
- [59] C. H. Olk and J. P. Heremans, "Scanning Tunneling Spectroscopy of Carbon Nanotubes," *J. Mater. Res.* **9**, 259 (Jan 1994).
- [60] L. G. Booshehri, C. L. Pint, G. D. Sanders, L. Ren, C. Sun, E. H. Házoz, J.-H. Kim, K. J. Yee, Y.-S. Lim, R. H. Hauge, C. J. Stanton, and J. Kono, "Polarization dependence of coherent phonon generation and detection in highly-aligned single-walled carbon nanotubes," In preparation (2010).